THE JOURNAL OF PHYSICAL CHEMISTRY LETTERS
A JOURNAL OF THE AMERICAN CHEMICAL SOCIETY

pubs.acs.org/JPCL

Perspective

Surface Plasmon–Photon Coupling in Lanthanide-Doped Nanoparticles

Xian Qin,* Albano N. Carneiro Neto, Ricardo L. Longo, Yiming Wu, Oscar L. Malta,* and Xiaogang Liu*

Cite This: *J. Phys. Chem. Lett.* 2021, 12, 1520–1541

Read Online

ACCESS | Metrics & More | Article Recommendations

ABSTRACT: Lanthanide-doped nanoparticles have great potential for energy conversion applications, as their optical properties can be precisely controlled by varying the doping composition, concentration, and surface structures, as well as through plasmonic coupling. In this Perspective we highlight recent advances in upconversion emission modulation enabled by coupling upconversion nanoparticles with well-defined plasmonic nanostructures. We emphasize fundamental understanding of luminescence enhancement, monochromatic emission amplification, lifetime tuning, and polarization control at nanoscale. The interplay between localized surface plasmons and absorbed photons at the plasmonic metal–lanthanide interface substantially enriches the interpretation of plasmon-coupled nonlinear photophysical processes. These studies will enable novel functional nanomaterials or nanostructures to be designed for a multitude of technological applications, including biomedicine, lasing, optogenetics, super-resolution imaging, photovoltaics, and photocatalysis.

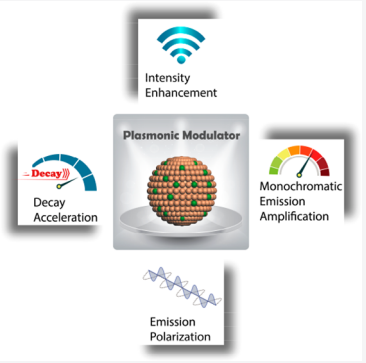

Lanthanide-activated photon upconversion, which represents a unique nonlinear optical phenomenon, has attracted enormous scientific and industrial interest since its discovery. This optical process is characterized by anti-Stokes emission that yields light at shorter wavelengths than the excitation spectrum upon sequential absorption of two or more photons. Unlike other anti-Stokes processes, such as two-photon absorption, lanthanide-activated photon upconversion overcomes constraints of high-power coherent excitation and stringent phase matching. In the early days following its discovery, upconversion materials in bulk crystal form were primarily used for infrared photon counting.[1] With rapid advances in nanomaterial synthesis, applications of upconversion nanoparticles (UCNPs) have been extended to biomedicine, including targeted therapeutics, optogenetics, and subdiffraction-limited bioimaging.[2−4] Compared with conventional organic dyes and quantum dots, UCNPs offer high photostability, large anti-Stokes shifts, zero-autofluorescence interference, and tunable upconversion luminescence under single-wavelength excitation, as well as deep-tissue imaging capability under near-infrared (NIR) excitation.

One of the most efficient upconversion systems is $NaYF_4$:Yb/Er, a material in which Yb^{3+} ions serve as sensitizers to absorb excitation energy and transfer it to Er^{3+} emitters.[5−7] However, the energy conversion efficiency of this system dampens significantly with decreasing particle size, primarily because of surface quenching of the excitation energy *via* nonradiative recombination. To this end, many strategies, such as shell passivation, dye sensitization, aliovalent doping, and strain engineering, have been employed to enhance upconversion emission intensity.[8−10]

Apart from emission intensity, many other features of UCNPs can be tuned for specific applications. For instance, it is possible to vary both emission color and lifetime by changing the doping concentration or by introducing aliovalent dopants.[11,12] Additionally, core–shell structure engineering has proven efficacious for controlling emission color.[13] Moreover, aliovalent doping can induce changes in crystal symmetry, resulting in polarized upconversion emission.[14]

Metal-supported localized surface plasmon resonance (LSPR) can drastically alter the electromagnetic environment of UCNPs and subsequently modulate their emission profiles without changing nanocrystal composition, size, or morphology. The interplay between surface plasmons and upconversion photons has been extensively examined theoretically on the basis of plasmon-dependent linear optical processes. However, surface plasmon-coupled photon upconversion at the single-particle level has been little examined, especially on plasmon-modulated energy transfer in lanthanide sublattices. Despite this challenge, research into key mechanisms

Received: December 8, 2020
Accepted: January 26, 2021

https://dx.doi.org/10.1021/acs.jpclett.0c03613
J. Phys. Chem. Lett. 2021, 12, 1520–1541

underlying plasmon-enhanced nonlinear photoluminescence has begun to develop momentum. In this Perspective we consider the most fundamental advances in surface plasmon−upconversion photon coupling. We first provide a survey of fundamentals governing plasmon-coupled upconversion processes, emphasizing recent examples using metal-supported LSPR to modulate optical properties. Second, we highlight developments in biomedical, anticounterfeiting, and photocatalytic applications of plasmon-coupled UCNPs, especially those offering stimulus-responsive multifunctional capability. We will delve into this rapidly evolving field and examine how advances in understanding at the single-particle level help bridge the divide between chemistry and disciplines such as materials science, nanophotonics, and optoelectronics.

Surface plasmon-coupled photon upconversion at the single-particle level has been little examined, especially on plasmon-modulated energy transfer in lanthanide sublattices. Despite this challenge, research into key mechanisms underlying plasmon-enhanced nonlinear photoluminescence has begun to develop momentum.

Surface Plasmon−Upconversion Coupling. Upon optical excitation, collective oscillations of free electrons occur at metal−dielectric interfaces (Figure 1a). The resulting surface plasmons generate an intense electromagnetic field, which can be used to modulate upconversion emission. To date, silver and gold nanomaterials are the most popular surface plasmon carriers, and their fundamental resonance modes can be tailored to match upconversion excitation or emission by changing the chemical composition, particle size, and shape of the metallic particle (Figure 1b). For example, gold nanoparticles show size- and shape-dependent absorption profiles (Figure 2a,b).[15] A hybridization model that shares a similar concept with molecular orbital theory can guide metal nanostructure design with predictable plasmon resonance wavelengths.[16] Specifically, plasmonic responses of metal nanoshells arise from plasmon coupling between metal spheres and cavities (Figure 2c). Next, we discuss the interaction between upconverters and surface plasmons in three areas: excitation absorption, energy transfer, and spontaneous emission.

Plasmon Resonance versus Excitation. For linear photoluminescence, the transition rate between two quantum states quadratically depends on the absolute square of the scalar product of electric field and dipole moment, as described with Fermi's golden rule:[17]

$$\gamma_{ij} = \frac{2\pi}{\hbar} |\langle i|\mathbf{E}\cdot\boldsymbol{\mu}|j\rangle|^2 \rho_f \tag{1}$$

where $\hbar$, $\mathbf{E}$, $\boldsymbol{\mu}$, and ρ_f are the reduced Planck's constant, local electromagnetic field, dipole moment, and density of optical states, respectively. Note that i and j represent two different quantum states. When resonating with incident light, metal-supported surface plasmons can confine large electromagnetic fields into subwavelength volumes, increasing the transition rate and spontaneous emission intensity. Given the nonlinearity of photon upconversion under low-power excitation, the emission intensity is proportional to $\mathbf{E}^{2n}$ for an upconversion process involving n photons. Emission at a shorter wavelength is more sensitive to the electric field because more photons participate in multiphoton upconversion than the number of photons available at longer wavelengths.

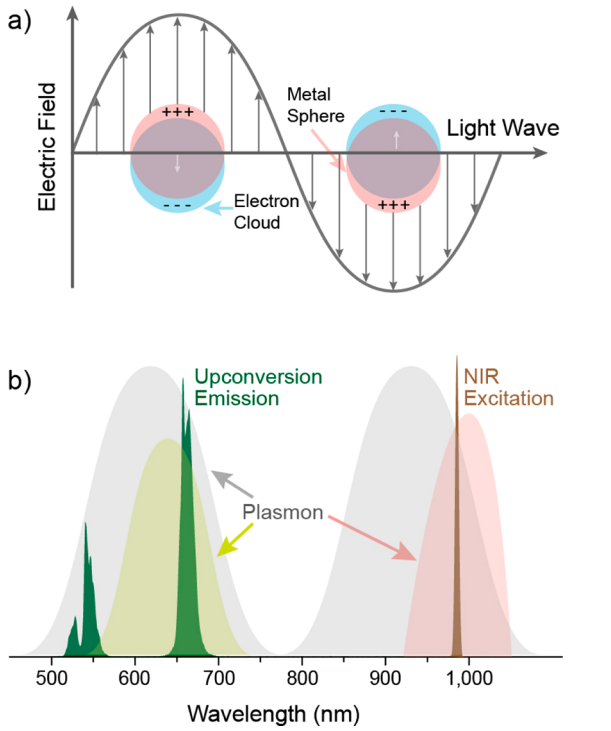

Figure 1. Schematics of (a) localized surface plasmon resonance in metal nanoparticles and (b) overlap between plasmon spectra of metallic nanoparticles and excitation or emission spectra of upconversion emitters.

Let us illustrate how plasmons change the absorption rate of a lanthanide sensitizer (*e.g.*, Yb^{3+}) in a UCNP, in close proximity to a spherical metallic nanoparticle. According to a recently developed model,[18,19] the maximum enhancement of the absorption rate can be achieved when UCNP and metallic nanoparticle are in contact (Figure 3). For a UCNP of radius R_p and a metallic nanoparticle with frequency-dependent polarizability $\alpha(\omega)$, the absorption rate is approximately enhanced by the factor of $(1 + 2|\alpha(\omega)|^2 R_p^{-6})$. A more direct expression of this enhancement factor in terms of geometric (f_{geo}) and frequency (f_ω) factors can be defined as

$$\left(1 + \frac{2\,|\alpha(\omega)|^2}{R_p^{\,6}}\right) = 1 + f_{geo} f_\omega \tag{2}$$

where

$$f_{geo} = \frac{2}{9}\left(\frac{a}{R_p}\right)^6, \quad f_\omega = \frac{\omega_p^{\,4}}{(\omega_R^{\,2} - \omega^2)^2 + (\Gamma_R\omega)^2} \tag{3}$$

For a spherical metallic nanoparticle with radius a, ω_R denotes surface plasmon frequency and Γ_R represents plasmon bandwidth at half-height. For instance, a metallic nanoparticle

https://dx.doi.org/10.1021/acs.jpclett.0c03613
J. Phys. Chem. Lett. 2021, 12, 1520−1541

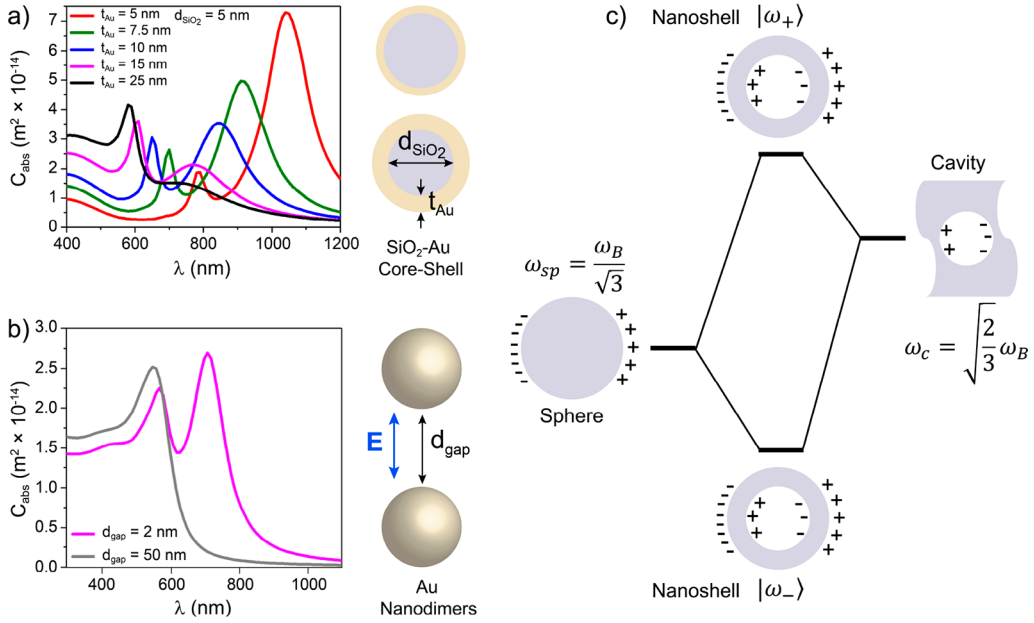

Figure 2. Absorption spectra of (a) SiO_2@Au core−shell nanostructures with different shell thicknesses and (b) Au nanoparticle dimers with different spacing. (c) Energy level diagram of a metallic nanoshell illustrating plasmon hybridization that originates from the coupling between the metallic sphere and the cavity. Reprinted from ref 15. Copyright 2019 American Chemical Society. Reprinted from ref 16. Copyright 2003 American Association for the Advancement of Science.

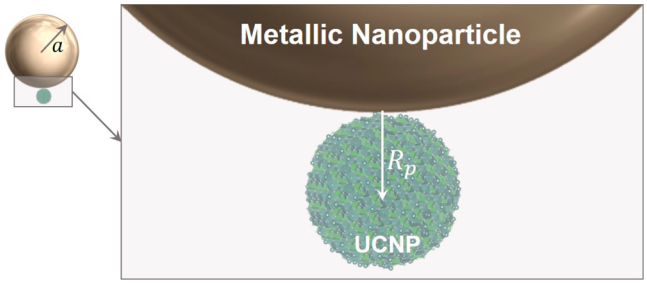

Figure 3. Schematic representation of a UCNP with radius R_p in contact with a metallic nanoparticle with radius a. This system lies on a flat metallic substrate, constituting a plasmonic cavity.

with a radius 3-fold larger than that of the UCNP ($a = 3R_p$) gives a geometric factor of $f_{geo} = 162$. For excitation frequencies ω not close to the surface plasmon frequency ω_R, the bandwidth contributions $\Gamma_R\omega$ are negligible and the frequency factor simplifies to $f_\omega \approx [\omega_p^2/(\omega_R^2 - \omega^2)]^2$. For gold, the bulk plasmon angular frequency ω_p is 1.30×10^{16} Hz (8.55 eV).[20] For Au nanoparticles with radii ranging from *ca.* 8 to 25 nm, the plasmon bandwidth Γ_R ranges from 0.32 to 0.34 eV and surface plasmon frequency ω_R ranges from 3.62×10^{15} to 3.53×10^{15} Hz (520 to 533 nm).[21] Considering the usual excitation frequency of 1.92×10^{15}Hz (980 nm), the bandwidth contributions $\Gamma_R\omega$ are indeed negligible and the frequency factor f_ω for these Au nanoparticles can be estimated as 320−370. The resulting enhancement factor reaches *ca.* 60 000. An increase of 5.6 times in the geometric factor ($f_{geo} = 910$) can be achieved when the size of the metallic nanoparticle is four times larger than that of the UCNP ($a = 4R_p$). On the other hand, an increase of the frequency factor can be achieved by choosing a metallic nanoparticle with surface plasmon frequency ω_R closer to the excitation frequency ω. For instance, if ω_R decreases to 3.16×10^{15} Hz (596 nm), then f_ω increases to *ca.* 720, which represents a 2-fold increase with respect to ω_R at 3.53×10^{15} Hz (533 nm). Another alternative consists of changing gold to silver nanoparticles because the latter has a higher bulk plasmon angular frequency ω_p of 1.46×10^{16} Hz (9.6 eV).[20] For a silver nanoparticle with $\omega_R = 3.16 \times 10^{15}$ Hz, its frequency factor f_ω is *ca.* 1145, 1.6-fold larger than that of the Au counterpart. In light of the large enhancement factor ($>10^5$) for common metallic nanoparticles and UCNPs, absorption saturation or eventual population inversion is likely to occur.

Plasmon Resonance versus Energy Transfer. The ability to control energy transfer between lanthanides in a given nanocrystal endows the nanocrystal with tunable upconversion characteristics.[22] Despite some progress, direct measurements of energy transfer remain challenging, largely because of complex transfer pathways between abundant 4f sublevels. Consequently, solving rate equations with experimentally measured parameters is the most commonly used method to probe energy-transfer rates between lanthanides. In 2013, by refining approximated steady-state rate equations with experimental measurements, Sun *et al.* theoretically decoupled different photophysical effects and found a 6-fold increase in resonant energy transfer from the $^2F_{5/2}$ state of Yb^{3+} to the $^4I_{11/2}$ state of Er^{3+} in β-$NaYF_4$:Yb/Er-coated gold pyramid arrays.[23] In a parallel study, Park's group reported that under low-power excitation at 980 nm, silver-supported plasmon resonance can enhance Yb^{3+} sensitization and facilitate energy transfer from the $^2F_{5/2}$ state of Yb^{3+} to the $^4I_{7/2}$ state of Er^{3+}, as corroborated by rate equations involving back-energy transfer.[24] The same group further determined the plasmon-induced enhancement in energy-transfer rates of nanosystems comprising silver nanogratings by examining the dynamics of both NIR and green emission.[25]

As with Yb−Er pairs, energy transfer within Yb−Yb or Er−Er dimers or their clusters is susceptible to surface plasmons.[26] That is also true for energy transfer between lanthanide and

https://dx.doi.org/10.1021/acs.jpclett.0c03613
J. Phys. Chem. Lett. 2021, 12, 1520−1541

transition metals in the presence of metal-cavity-supported surface plasmons.[27] Another exciting work on triply doped β-$NaYF_4$:Nd/Yb/Er nanoparticles showed that a rough gold film can generate ultrabroadband plasmons, inducing specific energy transfer between Yb and Er ions, but not between Nd and Yb ions.[28]

Full-field simulations can be combined with rate equations to study plasmon-coupled energy transfer. With simulated changes in the electromagnetic field and decay rate, one can calculate the relative population in different energy states to the ground state under a specific incident flux. For example, the magnitude of energy-transfer enhancement in gold nanosphere-coupled upconversion nanoparticles can be derived by solving a set of rate equations based on a simplified three-level energy diagram.[29] Moreover, in another study involving higher energy levels, populations of the six lowest excited states of Er^{3+} were calculated to predict changes in energy-transfer efficiency with gold nanosphere-supported plasmons.[30,31]

These theoretical works consider energy-transfer rates based on only dipole−dipole interactions that are commonly governed by the Förster mechanism. However, it has been demonstrated that other mechanisms, including exchange (Dexter's mechanism), dipole−quadrupole (quadrupole−dipole), and quadrupole−quadrupole interactions, could dominate the nonradiative energy transfer between lanthanide ions, depending on the sensitizer−activator distance.[32−35] In the next section, we discuss the Judd−Ofelt intensity parameters, overlap integrals, and 4f shielding effects, crucial to the determination of energy-transfer mechanisms.

Energy-Transfer Rates. The energy-transfer rates between lanthanide ions can be calculated by taking into account the dipole−dipole (W_{d-d}), dipole−quadrupole (W_{d-q}), quadrupole−quadrupole (W_{q-q}), exchange (W_{ex}), and magnetic dipole−magnetic dipole (W_{md-md}) interactions.[32,33,35] We treat energy-transfer rates separately from level populations in a rate equation model. Consequently, the calculated pairwise energy-transfer rates cannot be directly compared to the ones obtained from the model wherein energy-transfer rates and level population are correlated. Note that we focus on only the statistical average energy-transfer rates $\langle W\rangle$.

The pairwise energy-transfer rates are expressed as

$$W_{d-d} = \frac{(1-\sigma_1^{D})^2(1-\sigma_1^{A})^2}{(2J_D^*+1)(2J_A+1)}\frac{4\pi}{3\hbar}\frac{e^4}{R^6}\left(\sum_K \Omega_K^D\langle\psi_D J_D\|U^{(K)}\|\psi_D^* J_D^*\rangle^2\right)\times\left(\sum_K \Omega_K^A\langle\psi_A^* J_A^*\|U^{(K)}\|\psi_A J_A\rangle^2\right)F \quad (4)$$

$$W_{d-q,q-d} = \frac{(1-\sigma_1^{D,A})^2(1-\sigma_2^{A,D})^2}{(2J_D^*+1)(2J_A+1)}\frac{\pi}{\hbar}\frac{e^4}{R^8}\langle f\|C^{(2)}\|f\rangle^2 \times\left[\left(\sum_K \Omega_K^D\langle\psi_D J_D\|U^{(K)}\|\psi_D^* J_D^*\rangle^2\right)\langle r^2\rangle_A^2\langle\psi_A^* J_A^*\|U^{(2)}\|\psi_A J_A\rangle^2 + \left(\sum_K \Omega_K^A\langle\psi_A J_A\|U^{(K)}\|\psi_A^* J_A^*\rangle^2\right)\langle r^2\rangle_D^2\langle\psi_D^* J_D^*\|U^{(2)}\|\psi_D J_D\rangle^2\right]F \quad (5)$$

$$W_{q-q} = \frac{(1-\sigma_2^{D})^2(1-\sigma_2^{A})^2}{(2J_D^*+1)(2J_A+1)}\frac{28\pi}{5\hbar}\frac{e^4}{R^{10}}\langle r^2\rangle_D^2\langle r^2\rangle_A^2 \langle f\|C^{(2)}\|f\rangle^4\langle\psi_D J_D\|U^{(2)}\|\psi_D^* J_D^*\rangle^2\times\langle\psi_A^* J_A^*\|U^{(2)}\|\psi_A J_A\rangle^2 F \quad (6)$$

$$W_{ex} = \frac{2\pi}{\hbar}\left[\left(\frac{e^2}{R}\right)\rho_{f-f}^2\right]^2 F \quad (7)$$

$$W_{md-md} = \frac{(1-\sigma_1^{D})^2(1-\sigma_1^{A})^2}{(2J_D^*+1)(2J_A+1)}\frac{4\pi}{3\hbar}\frac{\mu_B^4}{R^6} \langle\psi_D J_D\|L+2S\|\psi_D^* J_D^*\rangle^2\langle\psi_A^* J_A^*\|L+2S\|\psi_A J_A\rangle^2 F \quad (8)$$

where R is the distance between lanthanide donor (sensitizer) and acceptor (activator) and the intensity parameters Ω_K are calculated using only the forced electric dipole contribution. The contribution from polarizability dynamic coupling is omitted because in Kushida's expressions the presence of the Ω_K parameters is due to the opposite parity configuration mixing by the odd components of the ligand field, similar to the Judd−Ofelt theory.[36] Importantly, these two contributions cannot be experimentally differentiated because their expressions have an identical form.[37,38]

The W_{q-q}, W_{ex}, and W_{md-md} rates are independent of the Ω_K parameters. It is worth noting that for the cases involving Er^{3+} emitters, the selection rules on the J quantum number do not allow the W_{md-md} mechanism. The ρ_{f-f} shown in eq 7 is the overlap integral between the 4f subshells of the lanthanide donors and acceptors, which decays exponentially with the donor−acceptor distance (R). As such, a drastic decrease in W_{ex} is expected.[39]

In eqs 4−8, $\langle\psi J\|\ \|\psi^* J^*\rangle$ are the reduced matrix elements that depend only on the lanthanide ion. Specifically, the $\langle\psi J\|L+2S\|\psi^*\ J^*\rangle$ can be calculated using wave functions in the intermediate coupling scheme,[40] and the $\langle\psi J\|U^{(K)}\|\psi^* J^*\rangle^2$ can be retrieved from ref 41. The $\langle r^k\rangle$ are 4f radial integrals[42,43] and the shielding factors $(1-\sigma_k)$ for the donor (sensitizer) and acceptor (activator), with k = 1 and 2, are given by[39,44]

$$(1-\sigma_k^{D,A}) = \rho(2\beta)^{k+1} \quad (9)$$

where ρ is the overlap integral between valence shells of the lanthanide−ligating atom in its first coordination sphere and $\beta = (1\pm\rho)^{-1}$. In eq 8, $\mu_B = e\hbar/(2m_e c)$ is the Bohr magneton.

The spectral overlap factor F expresses the energy mismatch conditions containing a sum over Franck−Condon factors. In the case of energy transfer between two lanthanide ions, the following analytical expression for F (in erg $^{-1}$) has been proposed:[35,38]

https://dx.doi.org/10.1021/acs.jpclett.0c03613
J. Phys. Chem. Lett. 2021, 12, 1520−1541

$$F = \frac{\ln(2)}{\sqrt{\pi}} \frac{1}{\hbar^2 \gamma_D \gamma_A} \left\{ \left[\left(\frac{1}{\hbar\gamma_D} \right)^2 + \left(\frac{1}{\hbar\gamma_A} \right)^2 \right] \ln(2) \right\}^{-1/2} \times \exp\left[\frac{1}{4} \frac{\left(\frac{2\Delta}{(\hbar\gamma_D)^2} \ln 2 \right)^2}{\left[\left(\frac{1}{\hbar\gamma_A} \right)^2 + \left(\frac{1}{\hbar\gamma_D} \right)^2 \right] \ln 2} - \left(\frac{\Delta}{\hbar\gamma_D} \right)^2 \ln(2) \right] \quad (10)$$

where $\hbar\gamma_D$ and $\hbar\gamma_A$ correspond to the bandwidths at half-height (in erg) of the donor and acceptor, respectively; Δ is the energy difference between donor and acceptor transitions, $\Delta = E_D - E_A$. For more details, we refer the reader to recent papers.[32,33,35,38]

The energy-transfer pathways are selected according to the energy mismatch conditions and the selection rules on J quantum number. For the multipolar mechanisms (W_{d-d}, W_{d-q}, and W_{q-q}), $|J - J'| \leq K \leq J + J'$ applies. For the exchange mechanism (W_{ex}) with isotropic contribution, there are no defined selection rules. For the magnetic dipole mechanism (W_{md-md}), the selection rule is $\Delta J = 0, \pm 1$ with the exception when $J = J' = 0$.

Considering that the energy-transfer rate strongly depends on the distance between lanthanide ions, one strategy to obtain an average photophysical property is to determine the average donor–acceptor energy-transfer rate $\langle W \rangle$ that will be employed in a set of rate equations for any given systems

$$\langle W \rangle = \sum_i C_i(R_i) W_i(R_i) \quad (11)$$

where the summation runs over the discrete distances between the acceptor and the donor until the ith distance shows negligible effects on the energy-transfer rate W_i, with $W_i = W_{d-d} + W_{d-q} + W_{q-q} + W_{ex} + W_{md-md}$ for a given donor–acceptor distance R_i, and C_i is the average occurrence number of donors per acceptor ion at layer-i. To obtain the C_i, we consider the cases of β-$NaYF_4$ and $LiYF_4$ nanocrystals codoped with Yb^{3+} and Er^{3+} ions (Figure 4), where C_i can be expressed as

$$C_i = \frac{\mathcal{N}(i)}{s \cdot \xi_{Ln}} \quad (12)$$

where $\mathcal{N}$ is the average counting number of donor–acceptor pairs present in layer-i (distance order in Table 1) and s is the number of host cation sites available for substitution by the lanthanide ion (ξ_{Ln} in fraction). This model can be applied for both forward (*e.g.*, Yb → Er) and backward (*e.g.*, Er → Yb) energy-transfer cases with different C_i coefficients, depending on the relative concentrations of donors and acceptors (Table 1). The same procedure applies to the $LiYF_4$ matrix and should be applicable to other crystalline hosts.

When using the shortest donor–acceptor distances, the calculated pairwise energy-transfer rates in β-$NaYF_4$ are higher than in the $LiYF_4$ lattice. According to the data listed in Tables 1 and 2, it is plausible to infer that the exchange and quadrupole–quadrupole interactions dominate. For the quadrupole–quadrupole interaction, this claim can be extended to longer distances, as discussed in ref 32.

When considering the overall upconversion emission yield of given metal–dielectric composites, an appropriate system of rate equations involving plasmonic effects is highly desired. In the presence of metallic plasmon resonance, for example, in a plasmonic cavity with known resonance modes, local field enhancement or Purcell effect may considerably change the absorption, decay (radiative and nonradiative), and nonradiative energy-transfer rates, affecting the energy level populations. Although researchers have stepped into the study of plasmon effect on the dipole–dipole interaction-mediated energy transfer, plasmon-induced changes in multipolar interactions deserve further research effort. Still, solving rate equations numerically or analytically considering detailed plasmonic effects is an effective means to probe the plasmon-coupled upconversion dynamics.

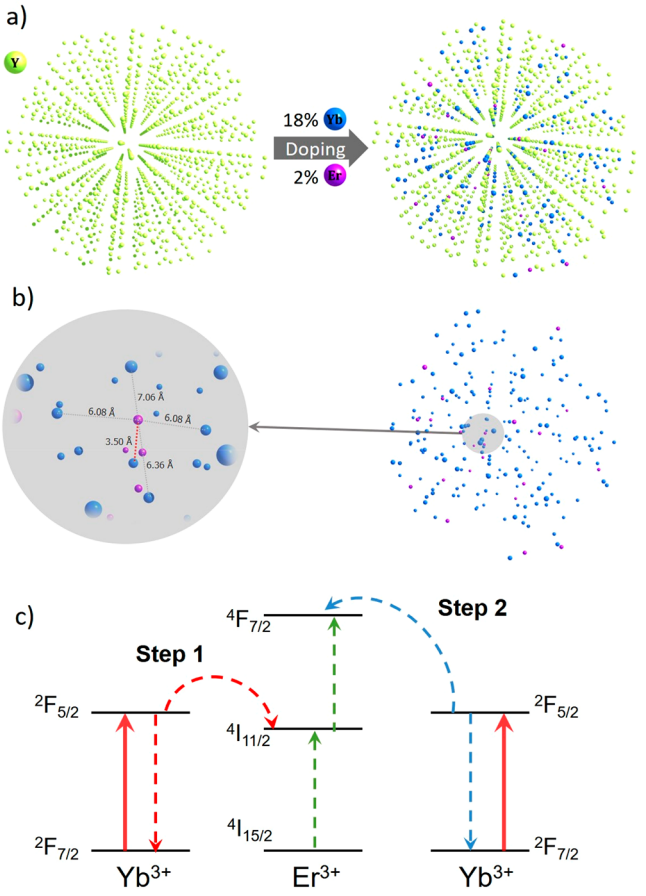

Figure 4. (a) Pristine yttrium sublattice (left) and doped (right) with Yb^{3+} and Er^{3+} ions (ξ_{Er} = 0.18 and ξ_{Er} = 0.02) in a β-$NaYF_4$ UCNP with a diameter of 6 nm. (b) Ytterbium and erbium sublattices (right) from where the donor–acceptor (Yb–Er) distances have been obtained for the calculation of the average occurrence number C_i using eq 12. The distance highlighted in red (3.50 Å) is the shortest donor–acceptor distance. (c) Simplified energy-level diagram involving energy-transfer steps 1 and 2 (Table 2). Solid arrows denote the absorption of Yb^{3+} ions.

Plasmon Resonance versus Emission. Let us consider the plasmonic effect on luminescence emission. When surface plasmon resonance overlaps with the emission wavelength of UCNPs, the electromagnetic local density of states can be tuned at emission states *via* the Purcell effect in the context of cavity quantum electrodynamics. This effect is expected to modify spontaneous emission rates because of their positive linear dependence on the local density of states, as manifested by Fermi's golden rule.

https://dx.doi.org/10.1021/acs.jpclett.0c03613
J. Phys. Chem. Lett. 2021, 12, 1520–1541

Table 1. Yb−Er Distances R (in Å) and C_i (Dimensionless) for the Forward (Yb → Er) and Backward (Er → Yb) Energy Transfer for Both $LiYF_4$ and β-$NaYF_4$ Nanocrystals Doped with Yb^{3+} (18%) and Er^{3+} (2%) Ions[a]

	$LiYF_4$			$NaYF_4$		
distance order (i)	R_i	C_i (Yb→Er)	C_i (Er→Yb)	R_i	C_i (Yb→Er)	C_i (Er→Yb)
1	**3.772**	0.331	0.039	**3.502**	0.098	0.011
2	**3.783**	0.326	0.038	**3.590**	0.106	0.012
3	5.230	0.311	0.036	**3.939**	0.317	0.037
4	5.270	0.312	0.036	**3.944**	0.316	0.037
5	6.418	0.301	0.035	6.077	0.870	0.102
6	6.457	0.304	0.036	6.350	0.286	0.033
7	6.479	0.517	0.060	6.358	0.281	0.033
8	6.517	0.303	0.035	7.014	0.629	0.073
9	6.565	0.608	0.071	7.059	0.561	0.065
10	6.595	0.885	0.103	7.093	0.477	0.056
11	7.371	0.297	0.035	7.096	0.275	0.032
12	7.477	0.292	0.034	7.242	0.281	0.033
13	8.307	0.283	0.033	7.245	0.280	0.033
14	8.353	0.282	0.033	8.790	0.256	0.030
15	8.542	0.280	0.033	8.795	0.259	0.030
16	8.581	0.280	0.033	9.340	1.544	0.180
17	9.778	0.334	0.039	9.454	0.527	0.062
18	9.795	0.271	0.032	9.456	0.522	0.061
19	9.869	0.547	0.064	9.551	0.257	0.030
20	9.898	0.266	0.031	9.560	0.270	0.032

[a]The distances in bold font are those smaller than 4 Å, where the W_{ex} and W_{q-q} mechanisms are by far the most relevant.

Table 2. Pairwise Energy-Transfer Rates W_i, with $W_i = W_{d-d} + W_{d-q} + W_{q-q} + W_{ex} + W_{md-md}$ for a Given Donor−Acceptor Distance R_i, Related to the Two Main Upconversion Steps[a]

	$LiYF_4$				$NaYF_4$			
	step 1		step 2		step 1		step 2	
Dist. ord. (i)	W_i (Yb→Er)	W_i (Er→Yb)	W_i (Yb→Er)	W_i (Er→Yb)	W_i (Yb→Er)	W_i (Er→Yb)	W_i (Yb→Er)	W_i (Er→Yb)
1	1.85×10^6	1.00×10^6	1.62×10^6	3.06×10^6	6.95×10^6	3.76×10^6	5.21×10^6	9.50×10^6
2	1.78×10^6	9.64×10^5	1.56×10^6	2.95×10^6	4.12×10^6	2.23×10^6	3.30×10^6	6.11×10^6
3	6.2×10^4	3.36×10^4	5.66×10^4	1.08×10^5	1.09×10^6	5.90×10^5	9.83×10^5	1.87×10^6
4	5.75×10^4	3.11×10^4	5.25×10^4	1.00×10^5	1.08×10^6	5.82×10^5	9.70×10^5	1.85×10^6
5	8.12×10^3	4.39×10^3	7.38×10^3	1.41×10^4	1.39×10^4	7.55×10^3	1.27×10^4	2.42×10^4
6	7.65×10^3	4.14×10^3	6.95×10^3	1.33×10^4	9.02×10^3	4.88×10^3	8.20×10^3	1.56×10^4
7	7.39×10^3	4.00×10^3	6.72×10^3	1.28×10^4	8.91×10^3	4.82×10^3	8.10×10^3	1.55×10^4
8	6.98×10^3	3.77×10^3	6.34×10^3	1.21×10^4	3.37×10^3	1.82×10^3	3.05×10^3	5.83×10^3
9	6.49×10^3	3.51×10^3	5.89×10^3	1.12×10^4	3.16×10^3	1.71×10^3	2.86×10^3	5.47×10^3
10	6.20×10^3	3.35×10^3	5.63×10^3	1.07×10^4	3.01×10^3	1.63×10^3	2.73×10^3	5.22×10^3
11	2.06×10^3	1.11×10^3	1.87×10^3	3.56×10^3	3.00×10^3	1.62×10^3	2.72×10^3	5.19×10^3
12	1.79×10^3	9.68×10^2	1.62×10^3	3.09×10^3	2.45×10^3	1.33×10^3	2.22×10^3	4.24×10^3
13	6.33×10^2	3.42×10^2	5.70×10^2	1.09×10^3	2.44×10^3	1.32×10^3	2.21×10^3	4.22×10^3
14	5.99×10^2	3.24×10^2	5.40×10^2	1.03×10^3	3.62×10^2	1.96×10^2	3.26×10^2	6.23×10^2
15	4.81×10^2	2.60×10^2	4.33×10^2	8.26×10^2	3.61×10^2	1.95×10^2	3.24×10^2	6.19×10^2
16	4.60×10^2	2.49×10^2	4.14×10^2	7.90×10^2	1.99×10^2	1.08×10^2	1.79×10^2	3.42×10^2
17	1.28×10^2	6.90×10^1	1.14×10^2	2.18×10^2	1.77×10^2	9.59×10^1	1.59×10^2	3.03×10^2
18	1.25×10^2	6.78×10^1	1.12×10^2	2.14×10^2	1.77×10^2	9.57×10^1	1.58×10^2	3.03×10^2
19	1.16×10^2	6.30×10^1	1.04×10^2	1.99×10^2	1.60×10^2	8.68×10^1	1.44×10^2	2.74×10^2
20	1.13×10^2	6.12×10^1	1.01×10^2	1.93×10^2	1.59×10^2	8.60×10^1	1.42×10^2	2.72×10^2
$\langle W \rangle$	**1.25×10^6**	**7.94×10^4**	**1.10×10^6**	**2.43×10^5**	**1.83×10^6**	**1.13×10^5**	**1.50×10^6**	**3.20×10^5**

[a]Both forward (Yb → Er) and backward (Er → Yb) energy transfer include the thermal mismatch correction $\exp(-|\Delta|)/(k_B T)$ when $\Delta < 0$. Δ is the energy mismatch that enters in the spectral overlap factor F. k_B is the Boltzmann's constant, and T was set to 300 K. The corresponding average total rate $\langle W \rangle$ is listed in the last row.

Beyond facilitating radiative decay, metal nanostructures can induce nonradiative decay by directly depopulating the excited states of lanthanide emitters, resulting in luminescence quenching. Plausible quenching mechanisms have been proposed based on experimental or theoretical evidence. For example, excited lanthanides may resonantly transfer their energy to proximal metal nanoparticles, generating surface plasmons that undergo damping within the metal nanostructures due to Ohmic losses. Another quenching pathway has been linked to the coupling of emissive energy to higher-order

https://dx.doi.org/10.1021/acs.jpclett.0c03613
J. Phys. Chem. Lett. 2021, 12, 1520−1541

plasmon modes that dissipate energy inside the metal objects.[45] As such, the coupling of plasmons with emitting photons leads to either an increase or decrease in upconversion emission intensity and quantum yield, depending on how surface plasmons modulate radiative and nonradiative decay processes. Note that the quantum yield η (or intrinsic quantum yield[46] denoted by Q_{Ln}^{Ln}) and emission intensity I are closely linked to decay rates, based on the following equations:

$$\eta = \gamma_r/(\gamma_r + \gamma_{nr}) \tag{13}$$

$$I = \hbar\omega\gamma_r = \hbar\omega\eta(\gamma_r + \gamma_{nr}) \tag{14}$$

where γ_r and γ_{nr} are the intrinsic radiative and nonradiative decay rates of a given emitter in the absence of plasmonic nanoparticles, respectively. $\hbar$ is the reduced Planck's constant, and ω is emission angular frequency.

To quantify enhancement in spontaneous emission rates, the ratio between plasmon-modified and free-space emission rates, known as the Purcell factor, has been widely used. However, cross-comparisons are not straightforward because of ambiguity in differentiating multiple decay pathways. In a review on metal−dielectric nanohybrids by Pelton,[47] two types of rate enhancement were explicitly defined by dissecting decay processes (Figure 5). Specifically, an emitter

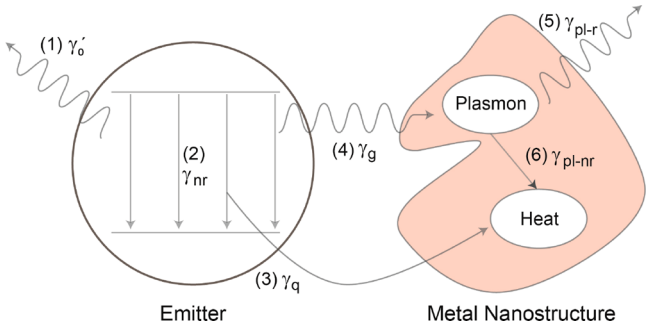

Figure 5. Schematics of decoupled decay pathways when an emitter is near metal nanostructures. γ_0', radiative decay to free space; γ_{nr}, intrinsic nonradiative decay of the emitter; γ_g, decay of the emitter that excites surface plasmons in the metal nanostructure; γ_q, metal-induced quenching; $\gamma_{pl\text{-}r}$, radiative decay of the meal; $\gamma_{pl\text{-}nr}$, nonradiative decay of the metal. Reprinted from ref 47. Copyright 2015 Springer Nature.

undergoes radiative decay to free space at a rate of γ_0' and excites surface plasmons at a rate of γ_g. It is also possible for the emitter to undertake intrinsic nonradiative decay (γ_{nr}) and metal-induced quenching (γ_q). For metal nanostructures, the excited plasmons may experience both radiative ($\gamma_{pl\text{-}r}$) and nonradiative ($\gamma_{pl\text{-}nr}$) decay. To satisfy the original definition of the Purcell factor,[48] Pelton used the expression $(\gamma_g + \gamma_0')/\gamma_0$ to estimate the overall modification of emission decay, where γ_0 is the emission rate of a given emitter in free space. To calculate the radiative enhancement factor, the formula $F_{rad} = \gamma_{far}/\gamma_0$ is appropriate, where $\gamma_{far} = \gamma_0' + \gamma_g\gamma_{pl\text{-}r}/(\gamma_{pl\text{-}r} + \gamma_{pl\text{-}nr})$ represents the far-field decay rate.

Although extensive investigations suggest that surface plasmons play a substantial role in each step of photon upconversion, the mechanism underlying surface plasmon−upconversion coupling remains unclear. An increase in electronic transition rate through plasmon coupling is likely to facilitate the decay of intermediate states, suppressing the

Although extensive investigations suggest that surface plasmons play a substantial role in each step of photon upconversion, the mechanism underlying surface plasmon−upconversion coupling remains unclear.

population of higher-lying energy states.[49] In this regard, the competition between plasmon-induced upconversion enhancement and quenching needs to be taken into consideration. This could be considered a distinct attribute of plasmon-modulated upconversion, compared to conventional photonic systems that do not involve real energy states, such as organic dyes and semiconductors. Another neglected feature is the spectral shift between the near- and far-field responses of plasmonic objects.[50] For example, the experimentally measured extinction coefficient is a far-field characteristic of a given plasmonic structure, while the interaction between the emitter and plasmon dominates in the near field. This suggests that further manipulation of plasmon−photon interaction is achievable by tuning off-resonance coupling. Additionally, upconversion enhancement observed at the nanoscale and macroscale may not be comparable because of the attenuation of both pump and emitted light during distant propagation.[51,52] The importance of these features was further examined by Rasskazov and co-workers using extended Mie theory, and the simulation results provided general guidelines for designing highly emissive upconversion nanosystems in which spherical Ag and Au nanoparticles are major surface plasmon carriers.[53]

Light emission modulation *via* surface plasmon-induced light scattering and trapping has been employed to explain the plasmon−photon coupling in lanthanide-activated upconversion nanocrystals. However, plasmon-associated hot electron injection and coherent energy transfer, coexisting with light scattering and trapping in metal−semiconductor heterostructures, have rarely been studied.[54,55] Notably, researchers have observed hot-electron-mediated upconversion emission from GaN/InGaN quantum wells and van der Waals heterostructures comprising plasmonic nanoparticles.[56,57] Moreover, plasmon-induced resonance energy transfer (PIRET) has been reported to extend the semiconductor's absorption spectrum to near- or even below-band gap energies.[58] We speculate that injection of hot electrons from plasmonic nanoparticles into the 4f states of lanthanides may occur when hot-electron energy matches the energy differences between lanthanide 4f excited states, analogous to the charge transfer from the host valence band to lanthanide ions. By comparison, blue-shifted, coherent PIRET from plasmonic objects to upconversion nanocrystals is less likely to occur because the dephasing time of lanthanide excited states is significantly longer than that of plasmons.

Upconversion Modulation. While parity-forbidden 4f−4f transitions within lanthanide ions induce weak absorption and long lifetimes, they also offer opportunities for emission enhancement and lifetime modulation. Moreover, controlling energy transfer within lanthanide sublattices or between nanoparticles is another useful approach to enhance emission. In this section, we review recent examples of plasmon-

https://dx.doi.org/10.1021/acs.jpclett.0c03613
J. Phys. Chem. Lett. 2021, 12, 1520−1541

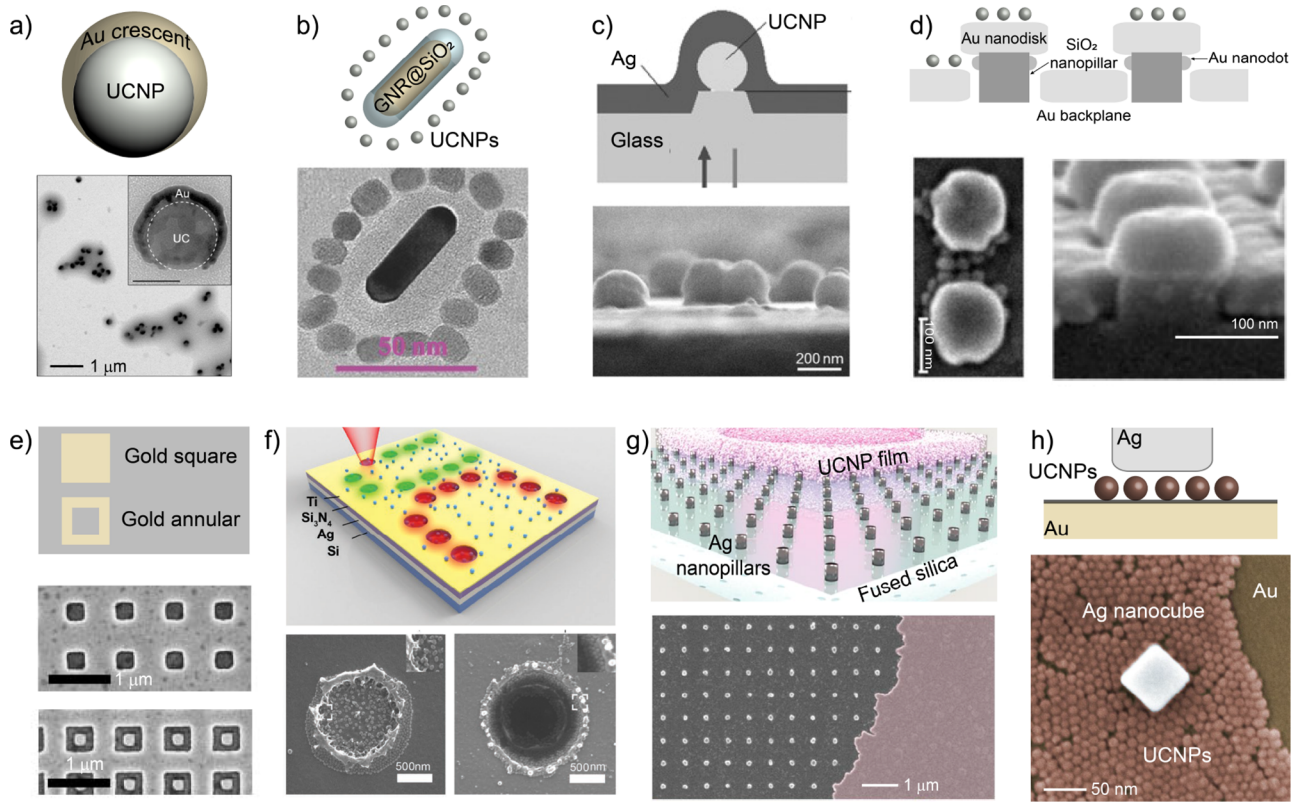

Figure 6. Schematic geometric structures (top panels) and SEM/TEM images (bottom panels) of various plasmon-coupled UCNPs. (a) UCNP@Au. (b) GNR@SiO_2−UCNP. (c) UCNP@Ag. (d) Multilayer design of Au nanodisks, SiO_2 nanopillars, Au backplanes, and UCNPs. (e) UCNP-deposited Au square/annular. (f) UCNP-deposited Ag nanocraters. (g) UCNP-deposited Ag nanopillars fused with silica. (h) Sandwiched design of Ag nanocube, UCNPs, and Au film. Reprinted from ref 62. Copyright 2017 American Chemical Society. Reprinted from ref 81. Copyright 2017 Wiley. Reprinted from ref 71. Copyright 2016 Wiley. Reprinted from ref 70. Copyright 2012 Wiley. Reprinted from ref 72. Copyright 2009 OSA Publishing. Reprinted from ref 68. Copyright 2019 Wiley. Reprinted from ref 79. Copyright 2019 Springer Nature. Reprinted from ref 64. Copyright 2019 Springer Nature.

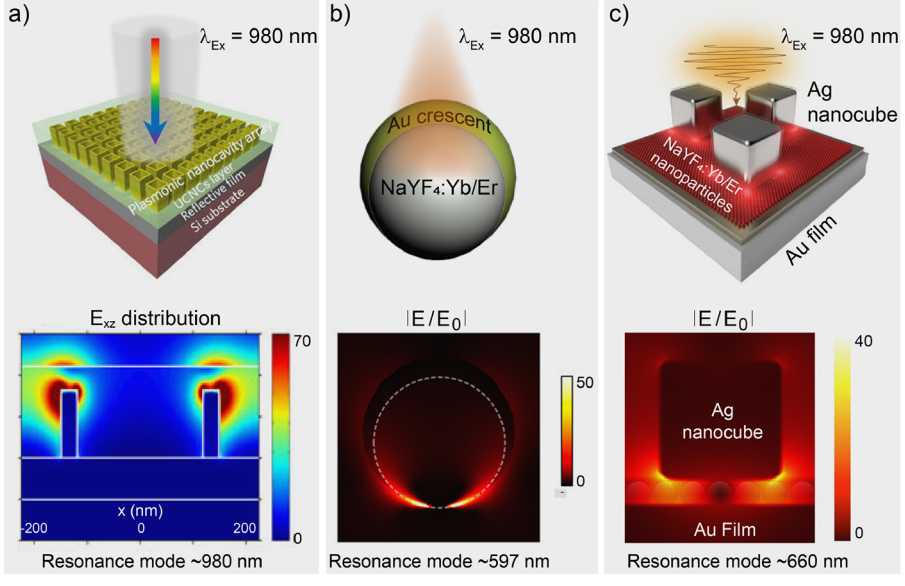

Figure 7. Simulated hotspot distribution within cavities of various metal−dielectric composites. (a) Gold box-like nanocavity. (b) Gold nanocrescent cavity. (c) Au−Ag nanogap cavity. Reprinted from ref 61. Copyright 2019 Wiley. Reprinted from ref 62. Copyright 2017 American Chemical Society. Reprinted from ref 64. Copyright 2019 Springer Nature.

mediated upconversion modulation in emission intensity, emission wavelength, and decay rate, as well as emission polarization.

Intensity Enhancement. The ability to detect weak emission by the unaided eye or using a simple instrument is essential for quick evaluation of phosphor performance.

https://dx.doi.org/10.1021/acs.jpclett.0c03613
J. Phys. Chem. Lett. 2021, 12, 1520−1541

Table 3. Upconversion Emission Enhancement at Various Wavelengths in Cavity-Based, Metal−Upconverter Nanocomposites

upconverter	plasmonics	resonance	power density	enhancement	ref
Er-doped sapphire (varied hole size)	Au hole array	1480 nm	2 W/cm^2	980 nm: 450-fold	72
$NaYF_4$:Yb/Er (25 nm)	Au-based 3D nanocavity	920 nm	300 W/cm^2	550 nm: 100-fold	70
				660 nm: 310-fold	
$NaYF_4$:Yb/Er (110 nm)	Au nanocavity arrays	980 nm	100 W/cm^2	540 nm: 30-fold	69
				660 nm: 30-fold	
Y_2O_3:Yb/Er@SiO_2	Ag nanocap	583 nm	9.6 × 10^3 W/cm^2	550 nm: 23-fold	73
(104 nm)		690 nm		670 nm: 48-fold	
$NaYF_4$:Gd/Yb/Tm@NaLuF4 (30 nm)	Ag cross-shape nanocavity	visible range	2 × 10^5 W/cm^2	345 nm: 170-fold	74
$NaYF_4$:Yb/Er (1.8 × 8 μm)	Ag cap	visible range	500 W/cm^2	4-fold	66
$NaYF_4$:Yb/Er (26 nm)	Au mesoporous film	550 nm	0.5 W/cm^2	541 nm: 32-fold	75
				656 nm: 41-fold	
$NaYF_4$:Yb/Ho/Ce	Ag nanocraters	538 nm	1.5 × 10^5 W/cm^2	538 nm: 1.98-fold	68
(25 × 34 nm)		650 nm		644 nm: 1.51-fold	
$NaYF_4$:Yb/Er	Ag−Au nanogap	660 nm	4 × 10^3 W/cm^2	554 nm: 1 600-fold	64
(20 nm)				660 nm: 10 100-fold	

Effects of size-, shape-, and composition-dependent plasmon resonance have been harnessed to enhance upconversion intensity over the past decade.[59,60] With the advent of advanced synthetic and fabrication techniques, metal−upconverter nanohybrids can be prepared in well-defined shapes and patterns, such as core−shell structures, caps, rods, pillars, and craters (Figure 6). Among these nanostructures, nanocavities have attracted intense interest because of their ability to yield large enhancement factors. In this subsection, we investigate the role of nanocavities in enhancing stimulated and spontaneous emission intensities from UCNPs. We take into account the spatial distribution of surface plasmons over a broad range of cavity geometries.

By revisiting Fermi's golden rule, see eq 1, one would expect large emission enhancement of lanthanide emitters in a strong electromagnetic field **E**, because emission intensity is proportional to $\mathbf{E}^{2n}$ for n-photon upconversion processes. Simulations based on finite-difference time-domain or transformation optics have allowed hotspots of high field intensity to be visualized near the irradiated nanocavity.[61−64] Notably, the distribution of hotspots at a given wavelength varies, depending on the geometric configuration of the nanocavity under study. For example, an intense 980 nm optical field was confined and extended outward around the upper part of a gold box-like nanocavity (Figure 7a).[61] In another case of an asymmetric, crescent-shaped nanocavity, even under off-resonant 980 nm irradiation, near-field excitation was concentrated at a tip region with a maximum enhancement factor of ∼50 (Figure 7b), with an enhanced electromagnetic field inside the crescent.[62] Hotspots were also computationally confirmed around the corners of silver nanocubes, spreading outward in the presence of narrow gaps (20 nm) between cubes and a gold substrate (Figure 7c).[64] The existence of hotspots was attributed to electromagnetic wave propagation in the form of surface plasmon polaritons toward sharp regions, ultimately leading to energy accumulation due to sudden loss of group velocities.[65]

Based on simulated near-field hotspot distribution, it is possible to precisely place upconverters within a hotspot of high field intensity to maximize energy harvesting. For example, Bang *et al.* achieved 16.1-fold emission enhancement by coating a nanocrescent (31.9 nm gap) onto a single 70 nm $NaYF_4$:Yb/Tm nanoparticle.[62] Recently, Wu *et al.* have reportedly achieved confinement of radiative upconversion emission into nanometric photonic hotspots of extremely high field intensity using gap-mode plasmonic nanocavities.[64] Nonlinear upconversion luminescence under low-power excitation was enhanced by a factor of ∼1 × 10^4, a more than 10-fold increase compared with early reported UCNP/plasmonic structures. This gap-mode plasmonic cavity enables planar fabrication that provides a robust, general, scalable solution for enhanced nonlinear luminescence. Compared to other plasmonic cavity designs, such as bowtie antennas made by electron-beam lithography, colloidally templated nanocavities are inexpensive, highly controllable, and ideal for large-scale, color-tunable nanophotonic applications.

Apart from enhanced excitation, Fermi's golden rule states that the electromagnetic environment dictates spontaneous emission decay through the local density of states—the number of photonic modes available for a given emitter. When considering the interplay between an emitter and a resonator, the Purcell factor relates the local density of optical states to the quality factor Q and mode volume V, enabling quantitative measurement of changes in spontaneous decay. The same consideration has also been extended to nanohybrids comprising nanocavities and UCNPs. When the fundamental mode of a nanocavity resonates with the lanthanide emission, researchers generally ascribe enhanced emission intensity and fast radiative decay rate to the Purcell effect.[64,66−68]

Table 3 summarizes the experimental results of plasmonic nanocavity-induced emission enhancement. The enhancement factor varies significantly from one nanocavity to another, such as 4-, 30-, and 310-fold increase in red emission when coupled with silver caps,[66] gold holes,[69] and a dot-on-pillar array,[70] respectively. Although the geometry of a particular nanocavity largely dictates spontaneous emission, it remains a formidable task to rigorously compare enhancement factors observed in different metal−upconverter nanohybrids. This challenge arises because of unstated experimental conditions, such as excitation power density and emission collection angle.[71] For instance, simulations show that an asymmetric nanocrescent structure radiates a large portion of emission toward the tip region,[62] while the Ag−Au nanogap directs emission light propagation along the norm of the Au film.[64]

https://dx.doi.org/10.1021/acs.jpclett.0c03613
J. Phys. Chem. Lett. 2021, 12, 1520−1541

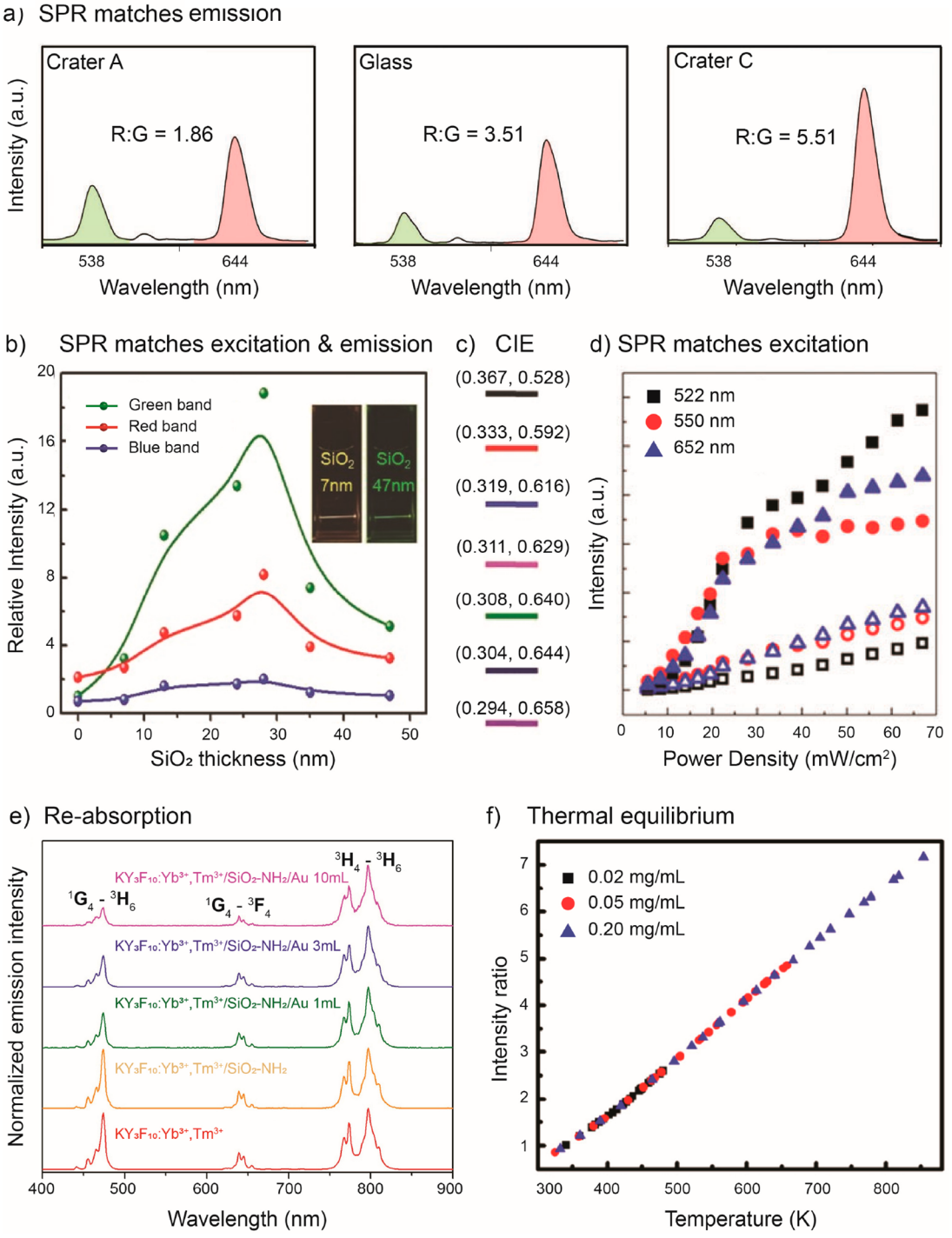

Figure 8. (a) Upconversion luminescence spectra of $NaYF_4$:Yb/Ho/Ce nanocrystals deposited on different nanocraters and glass. (b) Relative intensity of green, red, and blue emission as a function of SiO_2 coating thickness. Note that extracted emission from nanohybrids is normalized to the blue emission intensity of bare UCNPs. (c) Calculated CIE coordinates for bare UCNPs and six upconversion nanohybrids. (d) Upconversion emission of $NaYbF_4$:Yb/Er nanocrystals before (open) and after (solid) gold sputtering. (e) Emission spectra of core−shell nanohybrids with different SiO_2 thickness and of bare UCNPs. (f) Temperature-dependent intensity ratio between green and red of UCNPs deposited on a gold film. Reprinted from ref 68. Copyright 2019 Wiley. Reprinted from ref 81. Copyright 2017 Wiley. Reprinted from ref 82. Copyright 2010 The Royal Society of Chemistry. Reprinted from ref 84. Copyright 2017 Elsevier. Reprinted from ref 86. Copyright 2017 American Chemical Society.

Taken together, improved upconversion emission of lanthanides mainly originates from the strengthened electromagnetic field and increased local density of optical states due to proximal metal nanostructures, while the contribution from plasmon-enhanced energy transfer remains debatable. The resonance-wavelength tunability through structural design has made the nanocavity approach more versatile for drastic emission enhancement, compared with other approaches. Instead of matching either the absorption or emission wavelength, nanocavities with particular geometries can

https://dx.doi.org/10.1021/acs.jpclett.0c03613
J. Phys. Chem. Lett. 2021, 12, 1520−1541

provide multiple plasmon resonances that simultaneously overlap with absorption and emission bands of the lanthanide.[16,67] Despite these achievements, fundamental concerns, such as off-resonant effects and coupling in emitter ensembles, need to be addressed to further improve optical performance.

Monochromatic Emission Amplification. Upconversion emission with tunable wavelengths has unique utility for wavelength-specific applications, such as optogenetics that rely on a particular wavelength of light to activate or inhibit specific neurons. Unlike emission wavelength modulation of quantum dots and organic molecules, wavelength tuning of lanthanide emission is generally achieved by varying intensity ratios between different emission bands. For energy-transfer upconversion, enhancement at a particular wavelength can be attained by changing the host−activator combination, varying the lanthanide concentration, and introducing aliovalent dopants. Furthermore, by utilizing a new class of pulse duration-sensitive core−shell nanoparticles, researchers have demonstrated a versatile approach to dynamically fine-tuning emission wavelength and to constructing volumetric, full-color displays.[13]

Coupling upconversion emitters with plasmonic nanostructures presents an alternative strategy for emission wavelength modulation. A basic design is to enhance a selected emission wavelength that matches metal-supported plasmons. The enhancement is due to the coexistence of off-resonance local field enhancement and the Purcell effect. Selective enhancement in green and red emission has been demonstrated by coupling nanostructures with plasmon resonance at around 520 and 660 nm. For example, by coating $NaYF_4$:Yb/Er nanoparticles with a gold shell, Er^{3+} green emissions at 518 and 540 nm were selectively increased by ∼20 times compared to those without the gold shell, while other emission peaks remain essentially unaltered.[76] To enhance red or NIR emission, Au nanorods were designed with specific aspect ratios to maximize overlap between plasmon resonance and the lanthanide emissions at 660 and 805 nm.[77,78] Recently, Fernandez-Brave *et al.* demonstrated upconversion lasing at 660 nm using a plasmonic platform comprising Ag nanopillar arrays. The lattice constant of nanopillars was set to 460 nm, which yields a cavity-mode resonance at 660 nm.[79] The enhanced emission in the first biological window largely benefits biological applications where photon scattering and absorption in deep tissues present a major challenge. In addition to the aforementioned emission wavelengths, enhancement in upconverted high-energy emission such as blue, violet, and ultraviolet emissions has also been observed in well-defined metal−dielectric nanohybrids.[74,76,80]

Apart from boosting emission at a particular wavelength, it is possible to tune intensity ratios in a single set of UCNPs through structural engineering. For illustration, two sets of red-to-green ratios were detected simultaneously in $NaYF_4$:Yb/Ho/Ce nanocrystals under NIR irradiation when dispersed onto a specific sliver slab containing two types of nanocraters with different morphologies (Figures 6f and 8a).[68] For nanogaps formed between nanocubes and a substrate, its fundamental resonance mode can be subtly adjusted by varying the size of metal nanocubes. As a result, selective enhancement of green or red emissions from nanogap-containing Ag−Au structures is achievable by changing the size of Ag nanocubes.[64] In another hybrid system (Figure 6b), by taking advantage of the 795 nm longitudinal and 530 nm transverse plasmon resonances of gold nanorods, the Lei group not only demonstrated a plasmonic dual-enhancement in emission intensity from $NaGdF_4$:Nd/Yb/Er nanocrystals but also achieved precise control over the intensity ratio by varying the thickness of the SiO_2 spacer (Figure 8b,c).[81] It is noteworthy that one would expect a decrease in the red-to-green ratio only in the presence of excitation-matched plasmon resonance, because the high-order upconversion population benefits more from local field enhancement.[82]

Although the Purcell effect has been widely considered the major contributor to selective emission enhancement in most cases, other factors can regulate the color of upconverted emission. In 2011, a reabsorption mechanism was proposed for explaining the observed variation of green-to-red ratio in $NaYF_4$:Yb/Er@SiO_2 nanoparticles surrounded by gold nanoparticles (Figure 8d).[83] The authors argued that gold nanoparticles with resonance in the green-emission region can largely quench upconverted green emission *via* reabsorption by means other than Purcell enhancement. Such reabsorption-based color tuning has also been observed in Yb/Tm- and Yb/Er-codoped KY_3F_{10} nanoparticles attached by gold nanoparticles, as corroborated by an observed decrease in the integrated emission intensity of hybrid nanosystems and slightly changed decay rates of multiple transitions (Figure 8e).[84,85] In another study, a 36-fold enhancement in green emission and slightly suppressed red emission were ascribed to a plasmon-induced thermal effect that re-equilibrates the populations of $^2H_{11/2}$ and $^4S_{3/2}$ levels of Er^{3+} ions (Figure 8f).[86] Such a thermal re-equilibrium mechanism is a widely accepted working principle that governs the operation of upconversion nanothermometry.[87]

Although metal-supported plasmons have proven effective in controlling optical transitions within 4f-manifolds of lanthanides, mechanisms that underpin wavelength-selective enhancement or suppression remain largely ambiguous. This issue is largely due to the complex upconversion process and sophisticated coupling between plasmon resonance modes and abundant lanthanide energy levels. While these and other issues need to be investigated further, current knowledge calls for a careful examination of how to separate the effect of absorption enhancement from that of emission coupling.

Tunable Luminescence Lifetime. Owing to forced electric dipole transition, lanthanide luminescence is generally characterized by long emission lifetimes on the order of milliseconds. This long-lived emission feature has an added advantage because it allows an extensive modulation of spontaneous emission rates. Considerable research has demonstrated that interactions between a specific emitter and its local electromagnetic environment dictate spontaneous emission by changing the local electromagnetic density of states.[88] According to the Purcell effect described above, a significant increase in emission rate is expected when the electromagnetic field is spatially confined in a small optical resonator over a long period. As such, metal nanoparticles come into play because they can confine light within nanosized volumes in the form of localized surface plasmons. Despite strong damping, the use of localized surface plasmons for emission modulation remains an active research area.

In an early single-particle study, both plasmon-enhanced emission intensity and radiative decay in green and red emissions were observed when positioning gold nanospheres (540 nm resonance) in the close vicinity of a single UCNP.[89] The resulting lifetimes of green and red emissions are 30 and

https://dx.doi.org/10.1021/acs.jpclett.0c03613
J. Phys. Chem. Lett. 2021, 12, 1520−1541

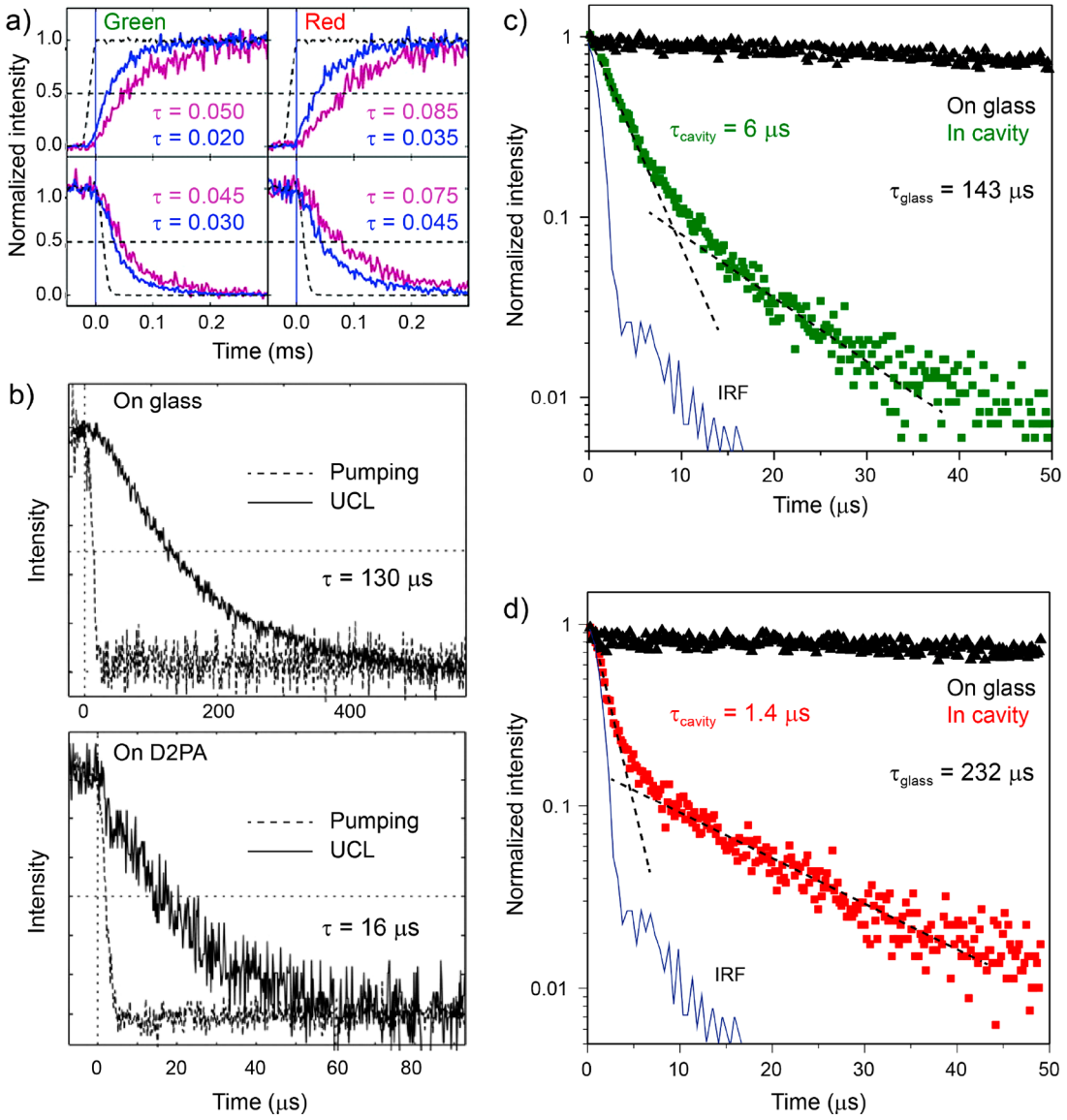

Figure 9. (a) Rise (upper) and decay times (lower) of green and red emissions of a single UCNP coupled to gold nanospheres. Violet and blue curves depict before and after coupling to the gold nanosphere, respectively. (b) Time-resolved measurement of upconversion luminescence in nanocrystals coated on glass (upper) and D2PA substrate (bottom). (c and d) Normalized time-resolved luminescence decay for UCNPs deposited on a glass slide (black) and between Ag−Au nanogaps at emission wavelengths of 554 and 660 nm. Reprinted from ref 89. Copyright 2010 American Chemical Society. Reprinted from ref 70. Copyright 2012 Wiley. Reprinted from ref 64. Copyright 2019 Springer Nature.

45 μs, respectively, while the corresponding values are 45 and 75 μs in the absence of gold nanospheres (Figure 9a). By constructing a sandwich-like structure, the Kagan group systematically studied the response of upconversion emission decay to variations in many structural and compositional parameters, including the thickness of the Al_2O_3 spacer, emitting ions, and the type of plasmonic metals.[90] With an optimized spacer thickness, the emission decay accelerated along with enhanced emission intensity from both Er^{3+} and Tm^{3+} emitters, irrespective of the metal composition (Au or Ag). The measured emission lifetime of $NaYF_4$:Yb/Er nanoparticles at 540 nm decreased from 298.2 to 144.8 μs when a Ag film coated with a 10 nm Al_2O_3 spacer was applied.

In addition to boosting excitation absorbance, metal nanocavities comprising a large number of "hotspots" can accelerate emission decay dynamics. In 2012, Zhang *et al.* reported a large decrease in lifetimes of $NaYF_4$:Yb^{3+}/Er^{3+} nanoparticles from 130 to 16 μs when spin-coated onto predesigned gold-based 3D nanocavity arrays that resonate at 920 nm (Figures 6d and 9b).[70] This short emission lifetime record was broken recently when Wu *et al.* achieved an upconversion superburst with a sub-2-μs lifetime within a plasmonic nanogap.[64] This improvement was made using a sandwiched Ag-UCNP-Au nanoresonator with ∼660 nm plasmon resonance, leading to a 166-fold decay rate enhancement accompanied by a four-order-of-magnitude increase in emission intensity (Figures 6h and 9c).

Despite successful demonstrations, it has been challenging to determine the Purcell factor, because emission decay needs to be quantitatively measured and this is not a trivial task by any means. Such a challenge is partly due to the requirement of decoupling the γ_{nr} and γ_q parameters from the overall measured lifetime. On the other hand, lifetime measurements of multiemitters may complicate emission analysis, because

https://dx.doi.org/10.1021/acs.jpclett.0c03613
J. Phys. Chem. Lett. 2021, 12, 1520−1541

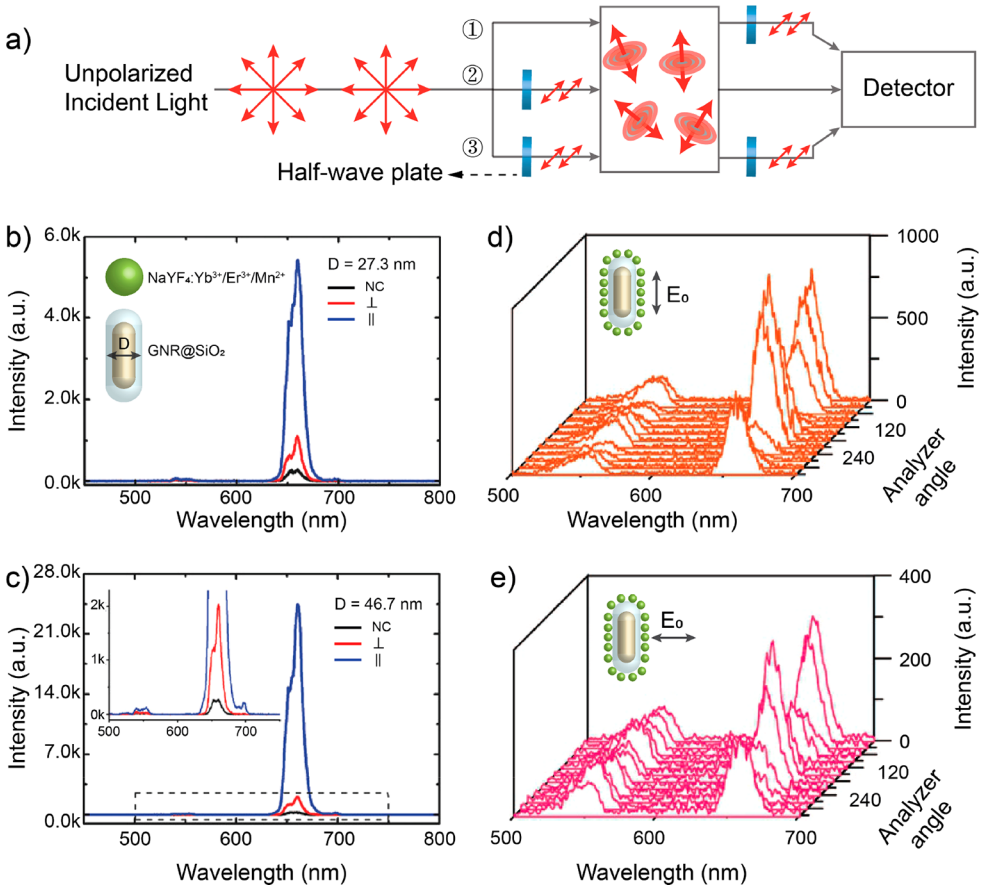

Figure 10. (a) Three general methods used for measuring polarized emission. (b and c) Emission spectra of upconversion nanocrystals, recorded before and after assembly with single Au nanorods of different diameters upon transverse (⊥) and longitudinal (||) polarized laser excitation. (d and e) Upconversion emission spectra, collected from different analyzer angles ($0-2\pi$) in metal−dielectric nanocomposites with excitation polarization parallel or perpendicular to the long axis of the nanorod. Reprinted from ref 100. Copyright 2017 Wiley. Reprinted from ref 101. Copyright 2017 Springer Nature.

the degree of plasmonic coupling varies with emitters located at different crystallographic sites. As such, single-emitter upconversion measurements enable further study of modified spontaneous emission in hybrid nanosystems.[91] Additionally, it should be noted that the ratio between emission intensities, as measured with and without metal nanostructures, is not equivalent to the Purcell factor in most cases. This arises because plasmon-enhanced intensity may originate from plasmon-enhanced absorption or plasmon-enhanced energy transfer instead of plasmon-enhanced emission alone. Furthermore, enhanced absorption is possible even for cases where metal-supported plasmons resonate with the lanthanide's emission.[89,90] It is becoming increasingly clear that methods to characterize individual contributions in the broader context of energy absorption, transfer, and emission should be explored further.

Emission Polarization Control. Polarized light has found various applications, from data storage to polarizing microscopy for diagnostics and bioimaging.[92] In principle, polarized light can be achieved by integrating an optical system with a specifically designed plate, such as a linear polarizer and a quarter-wave plate. However, complex instrumentation suffers from significant energy losses and largely hampers optical nanotechnology developments. Such a dilemma could be resolved using a nanophosphor that possesses inherent optical anisotropy, or that can be empowered through environmental intervention.

Although polarized emission has been extensively investigated, no detailed procedure for light polarization measurement exists in most cases. This deficiency has led to ambiguities in understanding the origin of polarization. Three methods are typically used to probe the anisotropy of emitted light (Figure 10a). The first method records emission as a function of polarization angle by rotating a half-wave plate in front of the collector. The resulting polarized emission is termed intrinsic polarization, because of unpolarized excitation. In general, the degree of detected anisotropy is trivial in lanthanide-doped nanocrystals because of the random orientation of transition dipoles. The second method involves controlling the polarization direction of incident light by adding a linear polarizer to the excitation laser. One would expect maximized emission intensity when the excitation polarization direction and transition dipole moment align parallel to each other. In this respect, the detected polarized emission is called excitation-imposed polarization. The third method uses two half-wave plates, resulting in an accumulation of both intrinsic and excitation-imposed polarization.

For upconversion emission, excitation-imposed polarized emission from lanthanides has been reported in Pr^{3+}-doped yttrium aluminum garnet crystals.[93] Similar excitation-imposed periodic changes in individual and overall upconversion

https://dx.doi.org/10.1021/acs.jpclett.0c03613
J. Phys. Chem. Lett. 2021, 12, 1520−1541

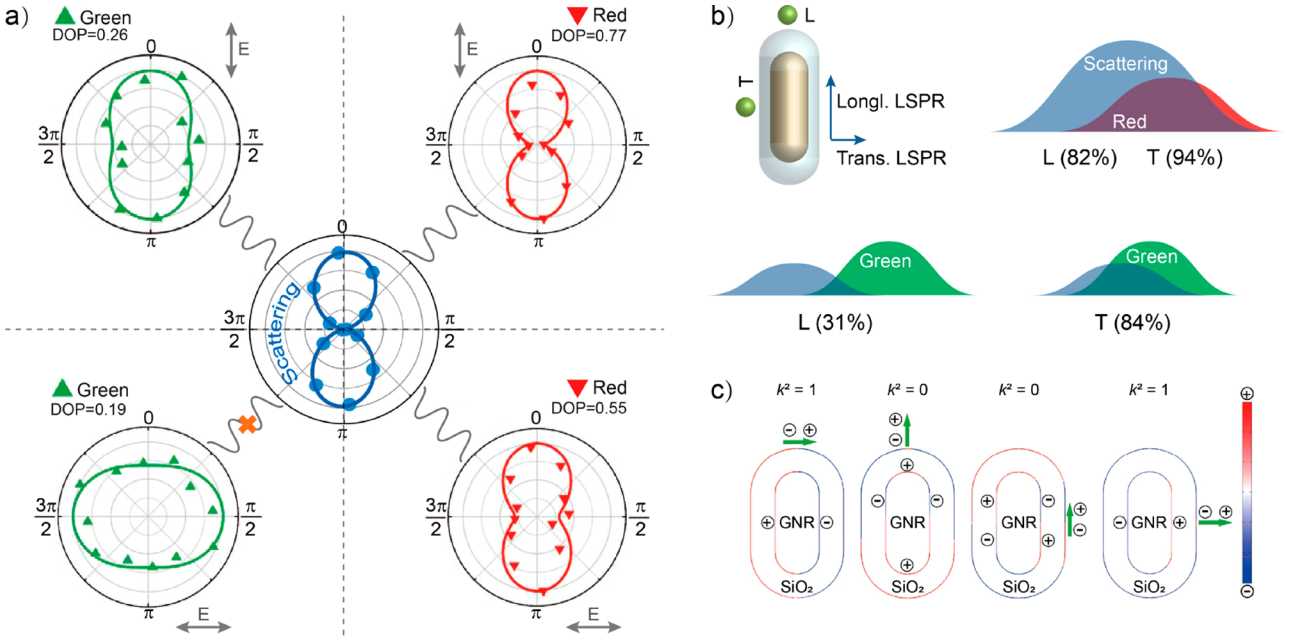

Figure 11. (a) Polar plots of scattering intensity of the Au nanorods, upconverted green emission, and red emission of the metal−dielectric nanohybrid, when excitation polarization is parallel and perpendicular to the long axis of the nanorods. (b) Schematic illustrations of spectral overlap between metal scattering and upconversion emissions. (c) Simulated charge distribution on the surfaces of the Au@SiO_2 nanorods irradiated by a green-emission dipole placed at different positions. Reprinted from ref 101. Copyright 2017 Springer Nature.

emission were detected in Yb^{3+}- and Er^{3+}-codoped $KMnF_3$ perovskite nanowires.[94] Apart from emission anisotropy induced by excitation, accumulative polarization has also been observed in a single nanorod, a nanodisk, or small aggregates, as evidenced by emission at various polarization angles.[14,95,96] There is a consensus that the orientation of optical transition dipoles relative to the principal axes of the lanthanide's coordination shell determines the anisotropic behavior of upconversion emission for both excitation-imposed and accumulative polarization.

Surface plasmons have attracted considerable attention for their effectiveness in increasing both overall and individual upconversion intensities. However, their role in polarization modulation was overlooked. Inspired by the discovery of plasmon-directed single-molecule emission,[97] efforts have been devoted to studying plasmon-enriched polarization behavior. As demonstrated in $NaYF_4$:Yb^{3+}/Er^{3+}-based nanodisks and nanoprisms at the single-particle level, excitation polarization- and orientation-induced variation of emission intensity can be magnified by coating UCNPs with gold shells.[98,99] Such enlarged intensity variations combined with high photostability simplify the emission-orientation mapping process and unleash the potential of UCNPs as orientation sensors for detection of rotational motion of biomolecules. In another study, the authors demonstrated that a transition from weak to strong coupling of emission intensity with laser polarization occurs when UCNPs are assembled with gold nanorods.[100] Notably, the magnitude of intensity variation is primarily determined by the direction of excitation polarization relative to the long axis of gold nanorods (Figure 10b,c).

In addition to excitation-imposed polarization, accumulative anisotropy could also be strengthened by placing lanthanide-doped nanocrystals in the vicinity of metal nanostructures, including nanorods,[101] nanopillar arrays,[79] and nanorectangular slot arrays.[102] By attaching sub-10 nm CaF_2:Yb^{3+}/Er^{3+} particles onto the surfaces of silica-coated gold nanorods, the Lei group reported polarized upconversion emissions at both green and red wavelengths from Er^{3+} ions upon excitation polarization either parallel or perpendicular to the long axis of the nanorod (Figure 10d,e).[101] Compared to the polarization degree of emission from pure nanoparticles (green, 0.11; red, 0.10), gold nanorod-supported surface plasmons offer 2.4- and 7.7-fold increases in green and red emissions, when excitation flux is parallel to the long axis of the nanorods. As a further step toward cumulative polarization modulation, Chen *et al.* showed that red emission from spherical $NaYF_4$:Yb^{3+}/Er^{3+} nanoparticles, which feature nonpolarized upconversion emission, can be selectively polarized by matching the surface plasmon resonance of the gold nanoantenna array with that of red emission.[102]

Despite observed plasmon-intensified or powered emission polarization in different nanohybrids, the underlying mechanism remains elusive, largely because of sophisticated couplings of emissive dipole moments with both the crystal field and the plasmon-strengthened optical field that the emitter experiences. Let us revisit the emission polarization behavior reported in ref 101 (Figure 10d,e). According to the polar plots (Figure 11a), red emission follows the polarization pattern of the scattering intensity of plasmonic nanorods, irrespective of the direction of excitation polarization. In contrast, the less polarized green emission reorients its direction perpendicular to the long axis upon perpendicular excitation. Having excluded the contribution of excitation polarization, researchers proposed a plasmon−emission coupling mechanism based on Förster resonance energy transfer.[103] Specifically, red emission largely overlaps the longitudinal plasmonic dipole at both positions L and T, while spectral overlap between green emission and the transverse plasmonic dipole at position T surpasses that achieved at position L. The simulated charge distribution indicates that constructive interference occurs between the emission dipole

https://dx.doi.org/10.1021/acs.jpclett.0c03613
J. Phys. Chem. Lett. 2021, 12, 1520−1541

and charge oscillation only at the T site with perpendicular direction, leading to polarized green emission along the transverse dipole of the nanorod (Figure 11b,c). Thus far, this is the only systematic investigation of plasmon-mediated polarization on upconversion emission of lanthanide-doped nanocrystals. Considering the complex upconversion process, a mechanistic research endeavor would reveal valuable principles for designing metal−upconverter nanohybrids with customized polarization behavior, such as circularly polarized upconversion.[104,105]

Emerging Applications. Advances in plasmon-modulated upconversion luminescence have developed rapidly during the past five years, and transformative changes enabled by plasmon−upconversion coupling in many fields are well underway. Interactions between dielectric and plasmonic materials, which largely determine upconversion luminescence behaviors, provide opportunities to address some of the major challenges in biomedical research, image encryption, and photocatalysis. This section discusses how to exploit these opportunities while accounting for cytotoxicity problems, heat-induced emission quenching, and complexities in encryption approaches, as well as multi-interactions in upconverter−metal−semiconductor photocatalysts.

Advances in plasmon-modulated upconversion luminescence have developed rapidly during the past five years, and transformative changes enabled by plasmon−upconversion coupling in many fields are well underway.

Biomedical Research. One of the most striking properties of UCNPs is their NIR responsiveness, allowing NIR photons to be converted into visible emission for deep tissue imaging at cellular resolution. Moreover, the broad tunability of their optical output enables multimodal imaging that combines color, intensity, and lifetime into simultaneous detection. Despite considerable effort, UCNP-based *in vivo* imaging techniques are limited by low emission intensity and requirements for high-concentration nanoparticles and high pumping power, which inevitably increase cytotoxicity and tissue damage. As an effective strategy to enhance luminescence, localized surface plasmon resonance was extended to upconversion-mediated bioimaging.[106,107] For instance, the Park group achieved high-contrast upconversion-mediated imaging of T24T cells using sandwich-like Au-$NaYF_4$:Yb/Er-Au nanoprobes.[106] Importantly, the required concentration of nanohybrids was 3 orders of magnitude less than that of pure UCNPs with the same level of brightness. This strategy largely reduced the adverse effects of excessive irradiation and nanoparticle overdose. In another study, Syamchand *et al.* demonstrated that Au-ZnO:Yb/Ho nanocomposites can produce bright upconversion and downshifting luminescence, providing a multimodal platform for visualizing interior structures of HeLa cells.[108]

Cancer therapy has been greatly enhanced by advances in imaging-guided diagnosis and treatment over the past decade. In particular, UCNPs have been widely employed to achieve imaging-guided photodynamic therapy (PDT) because of the spectral overlap between upconversion emission and absorption of photosensitizers commonly used for PDT. For instance, Chen *et al.* demonstrated how improved PDT efficacy from gold nanorod-conjugated UCNPs has made it possible to enhance *in vivo* treatment of OECM-1 oral cancer cells.[109] Improvement in PDT efficacy was attributed to enhancement in plasmon-coupled upconversion luminescence, which generates more reactive oxygen species.

Apart from photodynamic therapy, metal−upconverter nanohybrids have shown promise in photothermal therapy (PTT) because close contact between metal and upconverter can increase heat generation through direct deactivation of excited lanthanide emitters by resonantly transferring excitation energy to metal nanoparticles or *via* plasmon-facilitated nonradiative decay. Unlike plasmon-boosted upconversion emission in PDT, the performance of PTT-

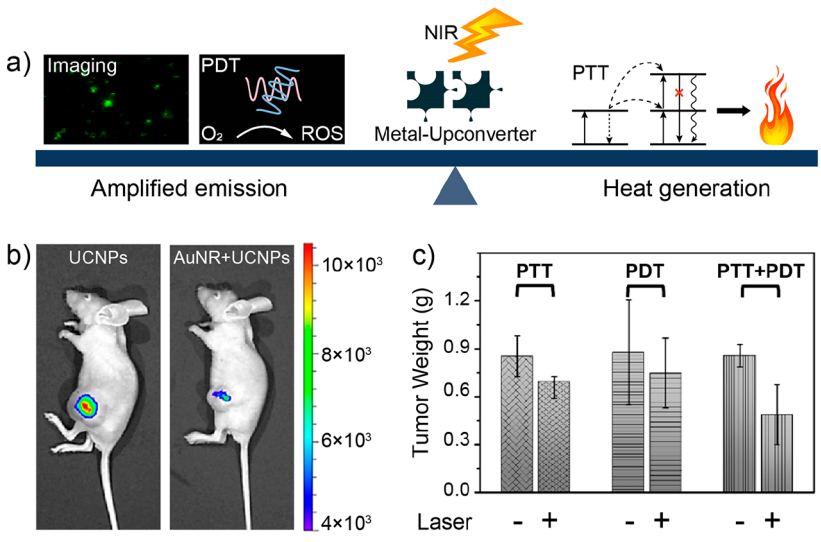

Figure 12. (a) Schematic illustration of optical imaging, photodynamic therapy, and photothermal therapy based on competition between plasmon-induced upconversion enhancement and quenching. (b) Luminescence images of animal models recorded using different nanoprobes. (c) Tumor weight plots under different experimental conditions. Reprinted from ref 106. Copyright 2018 Springer Nature. Reprinted from ref 114. Copyright 2018 American Chemical Society.

https://dx.doi.org/10.1021/acs.jpclett.0c03613
J. Phys. Chem. Lett. 2021, 12, 1520−1541

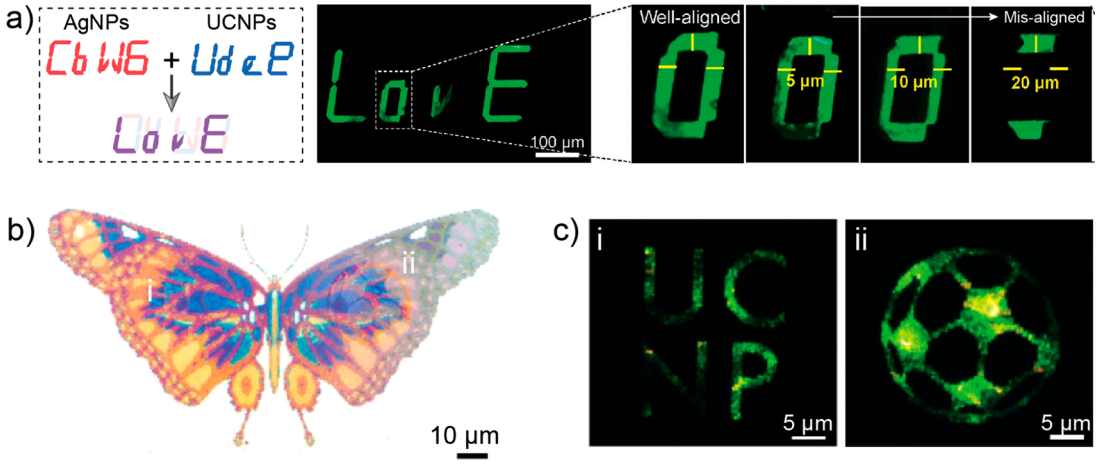

Figure 13. (a) Left: Schematic illustration of encrypted codes using Ag nanoparticles (AgNPs), UCNPs, and Ag−upconverter nanohybrids. Middle: Decrypted code pattern of Ag−upconverter nanohybrids when aligning AgNPs and UCNPs codes in a predesigned template. Right: Enlarged luminescent image of well-aligned and misaligned nanohybrids. (b) Optical micrograph of a plasmonic butterfly print under white-light irradiation. (c) Luminescence images of concealed letters and a football under near-infrared irradiation. Reprinted from ref 122. Copyright 2018 Wiley. Reprinted from ref 123. Copyright 2019 Wiley.

based treatment largely relies on the efficiency of metal-induced luminescence quenching. For instance, both resonant and nonresonant energy transfer from UCNPs to metal plasmonics have proven responsible for enhanced PTT treatment and thermally driven drug release.[110−113]

By harnessing dual effects of plasmon-induced luminescence enhancement and quenching, metal−upconverter nanohybrids can be used to perform imaging-guided dual-mode PDT and PTT of tumors *in vivo*. Although enhanced PTT performance is often accompanied by reduced imaging contrast and PDT efficacy, dual-mode phototherapy offers better treatment outcomes, as manifested by considerable shrinkage in tumor size after combined PDT−PTT treatment (Figure 12).[107,114,115] More specifically, luminescence quenching dominates when placing UCNPs close to small-sized plasmonic nanostructures (<10 nm), facilitating heat generation and improving PTT performance.[116,117] In contrast, by wedging a spacer such as a SiO_2 or polyelectrolyte layer with optimized thickness, upconversion quenching can be largely suppressed, subsequently enhancing PDT treatment.[51,118] Currently, the concept of metal−upconverter nanohybrids for biomedical application is still in its infancy, and a large number of technical obstacles need to be addressed before clinical trials can be undertaken, such as the need for highly luminescent, ultrasmall nanohybrids and optimal heat-induced upconversion quenching.

Image Encryption. Advances in technology and the growing use of the Internet have heightened potential problems with counterfeit goods. Image encryption presents an effective solution for anticounterfeiting measures, especially in the finance and healthcare sectors. Unique optical characteristics of UCNPs, such as multipeak emission, stimulus-dependent emission color, and tunable ratiometric intensity and decay lifetime can be used to encode banknotes or medical packaging, making forgery extremely difficult.[119,120] In essence, anticounterfeiting security features containing UCNPs can be directly printed onto any substrates of interest and visualized with a basic NIR microscope. Spectral imaging of the encoded pattern is also possible to provide stronger authentication for resources that require higher levels of security. However, owing to their low conversion efficiency, high concentrations of UCNPs are required to generate anticounterfeiting labels visible to the naked eye, which inevitably increases authentication cost.

In 2016, Park and co-workers demonstrated an efficient, cost-effective UCNP-based anticounterfeiting device by coupling a plasmonic Ag nanowire.[121] Specifically, sealed security labels containing sandwich-like Ag−upconverter composites emitted bright green light under NIR irradiation, while nonsealed labels barely responded to light stimulation because of loss of Ag nanowires and contamination of UCNPs when pulling out the preinserted adhesive tape. Importantly, reattachment of the adhesive tap failed to recover upconversion emission, thereby making forgery and counterfeiting challenging. In a further step toward high-level anticounterfeiting, the same group demonstrated the use of Ag−upconverter composites for information encryption at the micrometer scale, based on two conflicting features of plasmon-induced emission enhancement and quenching (Figure 13a).[122] Moreover, incorporation of a predesigned alignment guiding-layer guarantees one-time use of anticounterfeiting tags. More recently, nanoresonators of different sizes were used for multicolor upconversion-based image encryption.[123] Through the combination of luminescence enhancement and intrinsic plasmonic colors, a printed butterfly pattern exhibited a plasmonic color scheme under ambient white light, while green images of letters and a football appeared under NIR irradiation (Figure 13b,c). Apart from multilevel image encryption, surface plasmon coupling affords high emission brightness under low-pumping thresholds, which is inaccessible by plasmon-free nanophosphors. By combining surface plasmon resonance and dielectric superlensing, the pumping threshold for upconversion can be further reduced.[124,125]

Thus far, emission intensity and color are the two main optical elements that have been tuned *via* plasmonic coupling for anticounterfeiting measures. Meanwhile, other upconversion-related applications, including nanolasing,[79,126] solar cells,[127,128] and near-infrared photon detection,[124,128] have benefited mainly from plasmon-enhanced emission intensity.

https://dx.doi.org/10.1021/acs.jpclett.0c03613
J. Phys. Chem. Lett. 2021, 12, 1520−1541

Considering the plasmonic effect on upconversion lifetime and polarization, resonator−upconverter nanocomposites may find other utility, such as in photonic quantum computing and super-resolution nanoscopy.

Photocatalysis. For environmental photocatalysis associated with water splitting and pollutant remediation, an ideal force driving chemical reactions is solar energy. Conventionally, only the above-band gap excitation can activate semiconductor photocatalysts, limiting the utilization of solar energy.[129] To extend the light absorption range of semiconductors, lanthanide-doped nanocrystals have been broadly integrated into semiconductor-based photocatalysts to upconvert NIR to visible or ultraviolet light. Despite the conceptual demonstration, low conversion efficiency have restricted the practical application of upconversion nanocrystals. Importantly, realization of lanthanide upconversion under sunlight irradiation remains a formidable challenge.

Simultaneous integration of metal and upconversion nanoparticles has proven effective in improving the photocatalytic performance of semiconductor systems.[130−133] For instance, the TiO_2 electrodes integrated with Au and Er-doped nanoparticles displayed a 10-fold increase in photocurrent density under UV−vis−NIR illumination compared to pure TiO_2 photoanodes.[134] This suggests such composites can harvest low-energy photons and subsequently enhance conversion efficiency, benefiting photoelectrochemical water-splitting reactions. Another study reported 93-fold enhancement in photocurrent density by attaching UCNP-coupled hematite nanorods onto Au nanorod arrays.[135] In addition to water splitting, UCNP@TiO_2−Au composites also showed improved photocatalytic decomposition of methyl orange, as manifested by a high removal rate of 84% under 20 h NIR irradiation.[136]

Although researchers have demonstrated improved photocatalytic performance by integrating semiconductors with UCNPs and plasmonic nanoparticles, the underlying mechanism is still far from complete, mainly because of complex energy transfer between subcomponents. Upconverted emission can excite surface plasmons in metal nanostructures. Subsequent nonradiative dissipation of plasmon energy generates hot carriers that can be injected into empty resonance energy levels of proximal chemical reactants.[137] When UCNPs are placed in the vicinity of semicondutors, NIR excitation energy can be converted into UV−vis emission and transferred to semiconductors both radiatively and nonradiatively, generating electrons and holes in the semiconductors.[138−140] Notably, plasmon-coupled semiconductors can lead to improved photocatalytic performance through light scattering/trapping, hot electron injection, and coherent resonance energy transfer.[54]

Energy transfer can be manipulated by changing material geometry and composition. Let us revisit the plasmon- and upconversion-enhanced spectral response of TiO_2 photocatalysts.[134] For Tm-UCNP/Au/TiO_2 composites, both Au and TiO_2 components can receive upconverted energy. By replacing Tm^{3+} with Er^{3+} with improved spectral overlap, a large portion of upconverted energy is transferred to Au nanoparticles, boosting hot electron injection. In contrast, energy transfer from upconverters to seminconductors dominates in Au/UCNP/TiO_2 composites. To enhance our understanding of photocatalytic behavior, further research efforts are needed to decouple interactions among upconverters, plasmons, and semiconductors. Apart from serving as light converters, the intrinsic photocatalytic capability of lanthanide-doped upconversion nanocrystals is still unclear. The Cates group pointed out that the intensity of visible-to-UV phosphors is inadequate to drive catalytic degradation. The enhanced dye degradation is likely due to electron injection at the upconverter−semiconductor interface.[141] This situation applies only to visible-to-UV upconverters such as $Y_2SiO_5:Pr^{3+}$ and $Y_3Al_5O_{12}:Er^{3+}$, whereas NIR-to-visible/UV upconverters are more promising candidates for photocatalysis because of enhanced conversion efficiency.

Outlook. We are in the midst of an explosion of research activity to develop multifunctional UCNPs, ranging from applications for anticounterfeiting to bioimaging and cancer therapy. Over the past five years, research on surface plasmon−upconversion coupling has shifted from material synthesis to emission profile fine-tuning. With the help of localized surface plasmons, UCNPs become brighter and exhibit expanded features, such as tunable emission lifetime and polarization. Remote control over photophysical dynamics of emitters can be accomplished by means of a customized metallic medium. To date, a large amount of research data has provided guidance to engineering upconversion emission of metal−dielectric nanocomposites. Specifically, the most straightforward means of enhancing overall emission intensity is to match plasmon resonance with excitation wavelength. For selective enhancement or color tuning, plasmons should resonate with a targeted emission wavelength. Note that emission intensity enhancement *via* the Purcell effect is generally accompanied by accelerated radiative decay. In contrast, a shortened lifetime may result from metal-induced nonradiative decay. Generally, upon low-power excitation, one could expect significant enhancement of conversion efficiency in nanoconverters that exhibit low conversion efficiency. To maximize these optical signals, plasmons supported by nanocavities could be more prominent because of the presence of a highly intensified optical field, and full-field simulations could be valuable for prelocating these hotspots that a specific plasmonic structure can generate. When manipulating emission polarization, key factors include the geometric anisotropy of metal structures, the direction of the incident light, and positions of UCNPs relative to metal structures. Additionally, distances between upconverters and plasmonic structures need to be optimized to minimize metal-induced quenching.

While the conversion efficiency of UCNPs is steadily being improved, their expected performance for practical applications is still largely unknown because of a limited understanding of some of their key features. Complex energy-transfer behaviors have hindered the correlation between upconversion emission and surface plasmons. Challenges toward control over plasmon-induced energy transfer lie in understanding how plasmons affect each energy-transfer pathway. Some reports have attributed enhanced emitting states to an increased local density of states through Förster resonance energy transfer,[142,143] while conflicting evidence has also been published.[144,145] Experimentally, such studies require photophysical characterization at the single-particle level to decouple complex energy transfer among UCNPs in a given ensemble. Furthermore, optical characterization of single emitters will deepen our understanding of plasmon−emitter interactions, which remains a formidable task because of synthetic challenges in doping single emitters in lanthanide-based nanoparticles. Also, energy transfer from lanthanides to

https://dx.doi.org/10.1021/acs.jpclett.0c03613
J. Phys. Chem. Lett. 2021, 12, 1520−1541

metal nanoparticles is likely to complicate mechanistic studies. From a theoretical perspective, energy-transfer models that reckon with multipolar interactions between multiple donors and acceptors are highly desired.[35]

As in fundamental studies, many challenges remain in regard to practical applications of plasmon-coupled UCNPs. Notably, the short-range effectiveness of plasmons can cause inhomogeneous spatial signal distribution within large nanocrystals. To harness this powerful modulation, surface plasmons have been coupled with photonic effects.[146−149] Another concern is how to mitigate heat generation that originates from the relaxation of plasmonic hot carriers. Solving this heating problem will overcome thermal-induced energy loss and enable metal−dielectric nanocomposites for thermal-powered applications, such as photothermal therapy and drug delivery.[150] Additionally, low-cost material production will remain a critical factor for broad applications, and there is still significant potential for cost reduction by replacing precious metals with semiconductors as the plasmon carriers.[151,152] The coupling between semiconductor-mediated surface plasmons and upconversion photons has proven effective in modulating emission intensity and wavelength.[152−154] Notably, Zhou *et al.* discovered power-dependent plasmon-induced enhancement in $Cu_{2-x}S/MoO_3/NaYF_4$:Yb/Er composites, but not in the $Au/MoO_3/NaYF_4$:Yb/Er system.[155] The authors argued that electron diffusion from the semiconductor conduction band to lanthanide 4f states occurred under a high pump density (<0.7 W/mm^2) at 980 nm, while thermal quenching dominates when $Cu_{2-x}S$ was replaced with Au. The coexistence of challenges and opportunities is likely to motivate researchers and portends a bright future for plasmon-modulated upconversion. Over the next few years, it will be interesting to see how fundamental studies will continue to shape new frontiers in nanophotonics and biological applications.

AUTHOR INFORMATION

Corresponding Authors

Xian Qin − *Department of Chemistry, National University of Singapore, Singapore 117543, Singapore*; Email: chmqinx@nus.edu.sg

Oscar L. Malta − *Departamento de Química Fundamental, Universidade Federal de Pernambuco, Recife 50740-560, Brazil*; Email: oscar.malta@ufpe.br

Xiaogang Liu − *Department of Chemistry, National University of Singapore, Singapore 117543, Singapore; Center for Functional Materials, National University of Singapore Suzhou Research Institute, Suzhou 215123, China*; orcid.org/0000-0003-2517-5790; Email: chmlx@nus.edu.sg

Authors

Albano N. Carneiro Neto − *Phantom-g, CICECO-Aveiro Institute of Materials, Department of Physics, University of Aveiro, Aveiro 3810-193, Portugal*; orcid.org/0000-0003-2432-0992

Ricardo L. Longo − *Departamento de Química Fundamental, Universidade Federal de Pernambuco, Recife 50740-560, Brazil*; orcid.org/0000-0002-2738-7642

Yiming Wu − *Department of Chemistry, National University of Singapore, Singapore 117543, Singapore*

Complete contact information is available at: https://pubs.acs.org/10.1021/acs.jpclett.0c03613

Notes

The authors declare no competing financial interest.

ACKNOWLEDGMENTS

This work is supported by NUS NANONASH Programme (NUHSRO/2020/002/NanoNash/LOA; R143000B43114), Agency for Science, Technology and Research (A*STAR) (Grant No. A1983c0038), NRF Investigatorship programme (Award No. NRF-NRFI05-2019-0003), National Key R&D Program of China (2019YFC1604605), and National Natural Science Foundation of China (21771135). R.L.L. and O.L.M. are grateful to CNPq (Brazillian agency). A.N.C.N. acknowledges SusPhotoSolutions project (CENTRO-01-0145-FEDER-000005, Portugal) for financial support. This work was developed within the scope of the project CICECO-Aveiro Institute of Materials, UIDB/50011/2020 and UIDP/50011/2020, financed by Portuguese funds through the FCT/MEC and when appropriate cofinanced by FEDER under the PT2020 Partnership Agreement.

REFERENCES

(1) Bünzli, J. C. G. Rising Stars in Science and Technology: Luminescent Lanthanide Materials. *Eur. J. Inorg. Chem.* **2017**, *2017*, 5058−5063.

(2) Dong, H.; Du, S. R.; Zheng, X. Y.; Lyu, G. M.; Sun, L. D.; Li, L. D.; Zhang, P. Z.; Zhang, C.; Yan, C. H. Lanthanide Nanoparticles: From Design toward Bioimaging and Therapy. *Chem. Rev.* **2015**, *115*, 10725−10815.

(3) Xu, J.; Gulzar, A.; Yang, P.; Bi, H.; Yang, D.; Gai, S.; He, F.; Lin, J.; Xing, B.; Jin, D. Recent Advances in Near-Infrared Emitting Lanthanide-Doped Nanoconstructs: Mechanism, Design and Application for Bioimaging. *Coord. Chem. Rev.* **2019**, *381*, 104−134.

(4) Del Rosal, B.; Jaque, D. Upconversion Nanoparticles for in Vivo Applications: Limitations and Future Perspectives. *Methods Appl. Fluoresc.* **2019**, *7*, 022001.

(5) Auzel, F. Upconversion Processes in Coupled Ion Systems. *J. Lumin.* **1990**, *45*, 341−345.

(6) Page, R. H.; Schaffers, K. I.; Waide, P. A.; Tassano, J. B.; Payne, S. A.; Krupke, W. F.; Bischel, W. K. Upconversion-Pumped Luminescence Efficiency of Rare-Earth-Doped Hosts Sensitized with Trivalent Ytterbium. *J. Opt. Soc. Am. B* **1998**, *15*, 996−1006.

(7) Auzel, F. Upconversion and Anti-Stokes Processes with f and d Ions in Solids. *Chem. Rev.* **2004**, *104*, 139−174.

(8) Li, S.; Chen, H.; Zhao, Y.; Chen, Z.; Guo, E.-J.; Wu, Z.; Zhang, Y.; Tang, W.; Hao, J. Biaxial Strain-Induced Strong Enhancement of Upconversion Photoluminescence in Lanthanide-Doped Ferroelectric Thin Films. *J. Phys. D: Appl. Phys.* **2019**, *52*, 234002.

(9) Tessitore, G.; Mandl, G. A.; Brik, M. G.; Park, W.; Capobianco, J. A. Recent Insights into Upconverting Nanoparticles: Spectroscopy, Modeling, and Routes to Improved Luminescence. *Nanoscale* **2019**, *11*, 12015−12029.

(10) Wen, S.; Zhou, J.; Schuck, P. J.; Suh, Y. D.; Schmidt, T. W.; Jin, D. Future and Challenges for Hybrid Upconversion Nanosystems. *Nat. Photonics* **2019**, *13*, 828−838.

(11) Lu, Y.; Zhao, J.; Zhang, R.; Liu, Y.; Liu, D.; Goldys, E. M.; Yang, X.; Xi, P.; Sunna, A.; Lu, J.; et al. Tunable Lifetime Multiplexing Using Luminescent Nanocrystals. *Nat. Photonics* **2014**, *8*, 32−36.

(12) Qin, H.; Wu, D.; Sathian, J.; Xie, X.; Ryan, M.; Xie, F. Tuning the Upconversion Photoluminescence Lifetimes of $NaYF_4:Yb^{3+},Er^{3+}$ through Lanthanide Gd^{3+} Doping. *Sci. Rep.* **2018**, *8*, 12683.

(13) Deng, R.; Qin, F.; Chen, R.; Huang, W.; Hong, M.; Liu, X. Temporal Full-Colour Tuning through Non-Steady-State Upconversion. *Nat. Nanotechnol.* **2015**, *10*, 237−242.

(14) Zhou, J.; Chen, G.; Wu, E.; Bi, G.; Wu, B.; Teng, Y.; Zhou, S.; Qiu, J. Ultrasensitive Polarized Up-Conversion of Tm^{3+}-Yb^{3+} Doped β-$NaYF_4$ Single Nanorod. *Nano Lett.* **2013**, *13*, 2241−2246.

(15) Jauffred, L.; Samadi, A.; Klingberg, H.; Bendix, P. M.; Oddershede, L. B. Plasmonic Heating of Nanostructures. *Chem. Rev.* **2019**, *119*, 8087−8130.
(16) Prodan, E.; Radloff, C.; Halas, N. J.; Nordlander, P. A Hybridization Model for the Plasmon Response of Complex Nanostructures. *Science* **2003**, *302*, 419−422.
(17) Novotny, L.; Hecht, B. *Principles of Nano-Optics*, 2nd ed.; Cambridge, U.K., 2012.
(18) Carneiro Neto, A. N.; Couto dos Santos, M. A.; Malta, O. L.; Reisfeld, R. 2 - Effects of Spherical Metallic Nanoparticle Plasmon on 4f-4f Luminescence: A Theoretical Approach. *Nanophotonics* **2019**, 19−36.
(19) Couto dos Santos, M. A.; Malta, O. L.; Reisfeld, R. Modeling the Influence of Silver Nanoparticles on the f-f Luminescence of the EuEDTA Complex in the Polyvinylpirrolidone Polymer. *J. Lumin.* **2016**, *170*, 271−274.
(20) Blaber, M. G.; Arnold, M. D.; Ford, M. J. Search for the Ideal Plasmonic Nanoshell: The Effects of Surface Scattering and Alternatives to Gold and Silver. *J. Phys. Chem. C* **2009**, *113*, 3041−3045.
(21) Link, S.; El-Sayed, M. A. Size and Temperature Dependence of the Plasmon Absorption of Colloidal Gold Nanoparticles. *J. Phys. Chem. B* **1999**, *103*, 4212−4217.
(22) Qin, X.; Xu, J.; Wu, Y.; Liu, X. Energy-Transfer Editing in Lanthanide-Activated Upconversion Nanocrystals: A Toolbox for Emerging Applications. *ACS Cent. Sci.* **2019**, *5*, 29−42.
(23) Sun, Q. C.; Mundoor, H.; Ribot, J. C.; Singh, V.; Smalyukh, I. I.; Nagpal, P. Plasmon-Enhanced Energy Transfer for Improved Upconversion of Infrared Radiation in Doped-Lanthanide Nanocrystals. *Nano Lett.* **2014**, *14*, 101−106.
(24) Lu, D.; Cho, S. K.; Ahn, S.; Brun, L.; Summers, C. J.; Park, W. Plasmon Enhancement Mechanism for the Upconversion Processes in $NaYF_4$:Yb^{3+},Er^{3+} Nanoparticles: Maxwell versus Förster. *ACS Nano* **2014**, *8*, 7780−7792.
(25) Lu, D.; Mao, C.; Cho, S. K.; Ahn, S.; Park, W. Experimental Demonstration of Plasmon Enhanced Energy Transfer Rate in $NaYF_4$:Yb^{3+},Er^{3+} Upconversion Nanoparticles. *Sci. Rep.* **2016**, *6*, 18894.
(26) Mauser, N.; Piatkowski, D.; Mancabelli, T.; Nyk, M.; Mackowski, S.; Hartschuh, A. Tip Enhancement of Upconversion Photoluminescence from Rare Earth Ion Doped Nanocrystals. *ACS Nano* **2015**, *9*, 3617−3626.
(27) Wang, Y.; Nan, F.; Cheng, Z.; Han, J.; Hao, Z.; Xu, H.; Wang, Q. Strong Tunability of Cooperative Energy Transfer in Mn^{2+}-Doped (Yb^{3+},Er^{3+})/$NaYF_4$ Nanocrystals by Coupling with Silver Nanorod Array. *Nano Res.* **2015**, *8*, 2970−2977.
(28) Wang, Y.; Yang, Z.; Ma, Y.; Chai, Z.; Qiu, J.; Song, Z. Upconversion Emission Enhancement Mechanisms of Nd^{3+}-Sensitized $NaYF_4$:Yb^{3+},Er^{3+} Nanoparticles Using Tunable Plasmonic Au Films: Plasmonic-Induced Excitation, Radiative Decay Rate and Energy-Transfer Enhancement. *J. Mater. Chem. C* **2017**, *5*, 8535−8544.
(29) Esteban, R.; Laroche, M.; Greffet, J. J. Influence of Metallic Nanoparticles on Upconversion Processes. *J. Appl. Phys.* **2009**, *105*, 033107.
(30) Fischer, S.; Hallermann, F.; Eichelkraut, T.; von Plessen, G.; Krämer, K. W.; Biner, D.; Steinkemper, H.; Hermle, M.; Goldschmidt, J. C. Plasmon Enhanced Upconversion Luminescence near Gold Nanoparticles-Simulation and Analysis of the Interactions. *Opt. Express* **2012**, *20*, 271−282.
(31) Fischer, S.; Hallermann, F.; Eichelkraut, T.; von Plessen, G.; Krämer, K. W.; Biner, D.; Steinkemper, H.; Hermle, M.; Goldschmidt, J. C. Plasmon Enhanced Upconversion Luminescence near Gold Nanoparticles - Simulation and Analysis of the Interactions: Errata. *Opt. Express* **2013**, *21*, 10606−10611.
(32) Carneiro Neto, A. N.; Moura, R. T.; Malta, O. L. On the Mechanisms of Nonradiative Energy Transfer between Lanthanide Ions: Centrosymmetric Systems. *J. Lumin.* **2019**, *210*, 342−347.
(33) Carneiro Neto, A. N.; Moura, R. T.; Shyichuk, A.; Paterlini, V.; Piccinelli, F.; Bettinelli, M.; Malta, O. L. Theoretical and Experimental Investigation of the Tb^{3+}→Eu^{3+} Energy Transfer Mechanisms in Cubic $A_3Tb_{0.90}Eu_{0.10}(PO_4)_3$ (A = Sr, Ba) Materials. *J. Phys. Chem. C* **2020**, *124*, 10105−10116.
(34) Shyichuk, A.; Câmara, S. S.; Weber, I. T.; Carneiro Neto, A. N.; Nunes, L. A. O.; Lis, S.; Longo, R. L.; Malta, O. L. Energy Transfer Upconversion Dynamics in YVO_4:Yb^{3+},Er^{3+}. *J. Lumin.* **2016**, *170*, 560−570.
(35) Malta, O. L. Mechanisms of Non-Radiative Energy Transfer Involving Lanthanide Ions Revisited. *J. Non-Cryst. Solids* **2008**, *354*, 4770−4776.
(36) Kushida, T. Energy Transfer and Cooperative Optical Transitions in Rare-Earth Doped Inorganic Materials. I. Transition Probability Calculation. *J. Phys. Soc. Jpn.* **1973**, *34*, 1318−1326.
(37) Moura, R. T.; Carneiro Neto, A. N.; Longo, R. L.; Malta, O. L. On the Calculation and Interpretation of Covalency in the Intensity Parameters of 4f-4f Transitions in Eu^{3+} Complexes Based on the Chemical Bond Overlap Polarizability. *J. Lumin.* **2016**, *170*, 420−430.
(38) Carneiro Neto, A. N.; Teotonio, E. E. S.; de Sá, G. F.; Brito, H. F.; Legendziewicz, J.; Carlos, L. D.; Felinto, M. C. F. C.; Gawryszewska, P.; Moura, R. T.; Longo, R. L.; et al. Chapter 310 - Modeling Intramolecular Energy Transfer in Lanthanide Chelates: A Critical Review and Recent Advances. *Handbook on the Physics and Chemistry of Rare Earths* **2019**, *56*, 55−162.
(39) Carneiro Neto, A. N.; Moura, R. T., Jr Overlap Integrals and Excitation Energies Calculations in Trivalent Lanthanides 4f Orbitals in Pairs Ln-L (L = Ln, N, O, F, P, S, Cl, Se, Br, and I). *Chem. Phys. Lett.* **2020**, *757*, 137884.
(40) Ofelt, G. S. Structure of the F6 Configuration with Application to Rare-Earth Ions. *J. Chem. Phys.* **1963**, *38*, 2171−2180.
(41) Carnall, W. T.; Crosswhite, H.; Crosswhite, H. M. *Energy Level Structure and Transition Probabilities in the Spectra of the Trivalent Lanthanides in LaF_3*. Argonne National Laboratory: Argone, IL, 1978.
(42) Edvardsson, S.; Klintenberg, M. Role of the Electrostatic Model in Calculating Rare-Earth Crystal-Field Parameters. *J. Alloys Compd.* **1998**, *275*−*277*, 230−233.
(43) Smentek, L. Theoretical Description of the Spectroscopic Properties of Rare Earth Ions in Crystals. *Phys. Rep.* **1998**, *297*, 155−237.
(44) Malta, O. L.; Brito, H. F.; Menezes, J. F. S.; Silva, F. R. G. E; Alves, S.; Farias, F. S.; de Andrade, A. V. M. Spectroscopic Properties of a New Light-Converting Device Eu(Thenoyltrifluoroacetonate)$_3$ 2(Dibenzyl Sulfoxide). A Theoretical Analysis Based on Structural Data Obtained from a Sparkle Model. *J. Lumin.* **1997**, *75*, 255−268.
(45) Khurgin, J. B.; Sun, G. Impact of Surface Collisions on Enhancement and Quenching of the Luminescence near the Metal Nanoparticles. *Opt. Express* **2015**, *23*, 30739−30748.
(46) Bünzli, J.-C. G. On the Design of Highly Luminescent Lanthanide Complexes. *Coord. Chem. Rev.* **2015**, *293*−*294*, 19−47.
(47) Pelton, M. Modified Spontaneous Emission in Nanophotonic Structures. *Nat. Photonics* **2015**, *9*, 427−435.
(48) Purcell, E. M. Spontaneous Emission Probabilities at Radio Frequencies. *Phys. Rev.* **1946**, *69*, 681.
(49) Wang, Z.; Gao, W.; Wang, R.; Shao, J.; Han, Q.; Wang, C.; Zhang, J.; Zhang, T.; Dong, J.; Zheng, H. Influence of SiO_2 Layer on the Plasmon Quenched Upconversion Luminescence Emission of Core-Shell $NaYF_4$:Yb,Er@SiO_2@Ag Nanocomposites. *Mater. Res. Bull.* **2016**, *83*, 515−521.
(50) Wang, Y.-L.; Mohammadi Estakhri, N.; Johnson, A.; Li, H.-Y.; Xu, L.-X.; Zhang, Z.; Alù, A.; Wang, Q.-Q.; Shih, C.-K. Tailoring Plasmonic Enhanced Upconversion in Single $NaYF_4$:Yb^{3+}/Er^{3+} Nanocrystals. *Sci. Rep.* **2015**, *5*, 10196.
(51) Feng, A. L.; You, M. L.; Tian, L.; Singamaneni, S.; Liu, M.; Duan, Z.; Lu, T. J.; Xu, F.; Lin, M. Distance-Dependent Plasmon-Enhanced Fluorescence of Upconversion Nanoparticles Using Polyelectrolyte Multilayers as Tunable Spacers. *Sci. Rep.* **2015**, *5*, 7779.

https://dx.doi.org/10.1021/acs.jpclett.0c03613
J. Phys. Chem. Lett. 2021, 12, 1520−1541

(52) Yin, Z.; Zhou, D.; Xu, W.; Cui, S.; Chen, X.; Wang, H.; Xu, S.; Song, H. Plasmon-Enhanced Upconversion Luminescence on Vertically Aligned Gold Nanorod Monolayer Supercrystals. *ACS Appl. Mater. Interfaces* **2016**, *8*, 11667−11674.
(53) Rasskazov, I. L.; Wang, L.; Murphy, C. J.; Bhargava, R.; Carney, P. S. Plasmon-Enhanced Upconversion: Engineering Enhancement and Quenching at Nano and Macro Scales. *Opt. Mater. Express* **2018**, *8*, 3787−3804.
(54) Wu, N. Plasmonic Metal-Semiconductor Photocatalysts and Photoelectrochemical Cells: A Review. *Nanoscale* **2018**, *10*, 2679−2696.
(55) Tang, H.; Chen, C.-J.; Huang, Z.; Bright, J.; Meng, G.; Liu, R.-S.; Wu, N. Plasmonic Hot Electrons for Sensing, Photodetection, and Solar Energy Applications: A Perspective. *J. Chem. Phys.* **2020**, *152*, 220901.
(56) Naik, G. V.; Welch, A. J.; Briggs, J. A.; Solomon, M. L.; Dionne, J. A. Hot-Carrier-Mediated Photon Upconversion in Metal-Decorated Quantum Wells. *Nano Lett.* **2017**, *17*, 4583−4587.
(57) Linardy, E.; Trushin, M.; Watanabe, K.; Taniguchi, T.; Eda, G. Electro-Optic Upconversion in van Der Waals Heterostructures via Nonequilibrium Photocarrier Tunneling. *Adv. Mater.* **2020**, *32*, 2001543.
(58) Li, J.; Cushing, S. K.; Meng, F.; Senty, T. R.; Bristow, A. D.; Wu, N. Plasmon-Induced Resonance Energy Transfer for Solar Energy Conversion. *Nat. Photonics* **2015**, *9*, 601−607.
(59) Wu, D. M.; García-Etxarri, A.; Salleo, A.; Dionne, J. A. Plasmon-Enhanced Upconversion. *J. Phys. Chem. Lett.* **2014**, *5*, 4020−4031.
(60) Park, W.; Lu, D.; Ahn, S. Plasmon Enhancement of Luminescence Upconversion. *Chem. Soc. Rev.* **2015**, *44*, 2940−2962.
(61) Jung, K. Plasmonic Nanocavity Array for Enhanced Upconversion Luminescence. *Bull. Korean Chem. Soc.* **2019**, *40*, 91−92.
(62) Bang, D.; Jo, E. J.; Hong, S.; Byun, J. Y.; Lee, J. Y.; Kim, M. G.; Lee, L. P. Asymmetric Nanocrescent Antenna on Upconversion Nanocrystal. *Nano Lett.* **2017**, *17*, 6583−6590.
(63) Li, A. H.; Liu, D.; Luo, W.; Wang, J.; Sun, Z. Engineering Upconversion Using Cavity Plasmonic Mode of Ag Hemishell Capped on $NaLuF_4$:Yb,Er@SiO_2 Nanosphere. *J. Lumin.* **2019**, *206*, 211−217.
(64) Wu, Y.; Xu, J.; Poh, E. T.; Liang, L.; Liu, H.; Yang, J. K. W.; Qiu, C. W.; Vallée, R. A. L.; Liu, X. Upconversion Superburst with Sub-2 es Lifetime. *Nat. Nanotechnol.* **2019**, *14*, 1110−1115.
(65) Luo, Y.; Pendry, J. B.; Aubry, A. Surface Plasmons and Singularities. *Nano Lett.* **2010**, *10*, 4186−4191.
(66) Yang, J.; Li, A. H.; Chen, C.; Sun, Z. Cavity Controlled Upconversion Luminescence in Ag-Capped $NaYF_4$:Yb,Er Micron Rod. *J. Lumin.* **2017**, *187*, 466−470.
(67) Hinamoto, T.; Sugimoto, H.; Fujii, M. Metal-Core/Dielectric-Shell/Metal-Cap Composite Nanoparticle for Upconversion Enhancement. *J. Phys. Chem. C* **2018**, *122*, 17465−17472.
(68) Feng, Z.; Hu, D.; Liang, L.; Xu, J.; Cao, Y.; Zhan, Q.; Guan, B. O.; Liu, X.; Li, X. Laser-Splashed Plasmonic Nanocrater for Ratiometric Upconversion Regulation and Encryption. *Adv. Opt. Mater.* **2019**, *7*, 1900610.
(69) Fisher, J.; Zhao, B.; Lin, C.; Berry, M.; May, P. S.; Smith, S. Spectroscopic Imaging and Power Dependence of Near-Infrared to Visible Upconversion Luminescence from $NaYF_4$:Yb^{3+},Er^{3+} Nanoparticles on Nanocavity Arrays. *J. Phys. Chem. C* **2015**, *119*, 24976−24982.
(70) Zhang, W.; Ding, F.; Chou, S. Y. Large Enhancement of Upconversion Luminescence of $NaYF_4$:Yb^{3+}/Er^{3+} Nanocrystal by 3D Plasmonic Nano-Antennas. *Adv. Mater.* **2012**, *24*, OP236−OP241.
(71) Li, A.-H.; Lü, M.; Guo, L.; Sun, Z. Enhanced Upconversion Luminescence of Metal-Capped $NaGd_{0.3}Yb_{0.7}F_4$:Er Submicrometer Particles. *Small* **2016**, *12*, 2092−2098.
(72) Verhagen, E.; Kuipers, L.; Polman, A. Field Enhancement in Metallic Subwavelength Aperture Arrays Probed by Erbium Upconversion Luminescence. *Opt. Express* **2009**, *17*, 14586−14598.
(73) Yamamoto, K.; Fujii, M.; Sowa, S.; Imakita, K.; Aoki, K. Upconversion Luminescence of Rare-Earth-Doped Y_2O_3 Nanoparticle with Metal Nano-Cap. *J. Phys. Chem. C* **2015**, *119*, 1175−1179.
(74) El Halawany, A.; He, S.; Hodaei, H.; Bakry, A.; Razvi, M. A. N.; Alshahrie, A.; Johnson, N. J. J.; Christodoulides, D. N.; Almutairi, A.; Khajavikhan, M. Enhanced UV Upconversion Emission Using Plasmonic Nanocavities. *Opt. Express* **2016**, *24*, 13999−14009.
(75) Qin, H.; Shamso, A. E.; Centeno, A.; Theodorou, I. G.; Mihai, A. P.; Ryan, M. P.; Xie, F. Enhancement of the Upconversion Photoluminescence of Hexagonal Phase $NaYF_4$:Yb^{3+},Er^{3+} Nanoparticles by Mesoporous Gold Films. *Phys. Chem. Chem. Phys.* **2017**, *19*, 19159−19167.
(76) Kannan, P.; Rahim, F. A.; Teng, X.; Chen, R.; Sun, H.; Huang, L.; Kim, D.-H. Enhanced Emission of $NaYF_4$:Yb,Er/Tm Nanoparticles by Selective Growth of Au and Ag Nanoshells. *RSC Adv.* **2013**, *3*, 7718−7721.
(77) Feng, A. L.; Lin, M.; Tian, L.; Zhu, H. Y.; Guo, H.; Singamaneni, S.; Duan, Z.; Lu, T. J.; Xu, F. Selective Enhancement of Red Emission from Upconversion Nanoparticles via Surface Plasmon-Coupled Emission. *RSC Adv.* **2015**, *5*, 76825−76835.
(78) Kannan, P.; Abdul Rahim, F.; Chen, R.; Teng, X.; Huang, L.; Sun, H.; Kim, D.-H. Au Nanorod Decoration on $NaYF_4$:Yb/Tm Nanoparticles for Enhanced Emission and Wavelength-Dependent Biomolecular Sensing. *ACS Appl. Mater. Interfaces* **2013**, *5*, 3508−3513.
(79) Fernandez-Bravo, A.; Wang, D.; Barnard, E. S.; Teitelboim, A.; Tajon, C.; Guan, J.; Schatz, G. C.; Cohen, B. E.; Chan, E. M.; Schuck, P. J.; et al. Ultralow-Threshold, Continuous-Wave Upconverting Lasing from Subwavelength Plasmons. *Nat. Mater.* **2019**, *18*, 1172−1176.
(80) Wang, L.; Guo, S.; Liu, D.; He, J.; Zhou, J.; Zhang, K.; Wei, Y.; Pan, Y.; Gao, C.; Yuan, Z.; et al. Plasmon-Enhanced Blue Upconversion Luminescence by Indium Nanocrystals. *Adv. Funct. Mater.* **2019**, *29*, 1901242.
(81) Kang, F.; He, J.; Sun, T.; Bao, Z. Y.; Wang, F.; Lei, D. Y. Plasmonic Dual-Enhancement and Precise Color Tuning of Gold Nanorod@SiO_2 Coupled Core-Shell-Shell Upconversion Nanocrystals. *Adv. Funct. Mater.* **2017**, *27*, 1701842.
(82) Zhang, H.; Xu, D.; Huang, Y.; Duan, X. Highly Spectral Dependent Enhancement of Upconversion Emission with Sputtered Gold Island Films. *Chem. Commun.* **2011**, *47*, 979−981.
(83) Li, Z.; Wang, L.; Wang, Z.; Liu, X.; Xiong, Y. Modification of $NaYF_4$:Yb,Er@SiO_2 Nanoparticles with Gold Nanocrystals for Tunable Green-to-Red Upconversion Emissions. *J. Phys. Chem. C* **2011**, *115*, 3291−3296.
(84) Runowski, M. Color-Tunable up-Conversion Emission of Luminescent-Plasmonic, Core/Shell Nanomaterials - KY_3F_{10}:Yb^{3+},Tm^{3+}/SiO_2-NH_2/Au. *J. Lumin.* **2017**, *186*, 199−204.
(85) Runowski, M.; Stopikowska, N.; Goderski, S.; Lis, S. Luminescent-Plasmonic, Lanthanide-Doped Core/Shell Nanomaterials Modified with Au Nanorods - Up-Conversion Luminescence Tuning and Morphology Transformation after NIR Laser Irradiation. *J. Alloys Compd.* **2018**, *762*, 621−630.
(86) Zhang, W.; Li, J.; Lei, H.; Li, B. Plasmon-Induced Selective Enhancement of Green Emission in Lanthanide-Doped Nanoparticles. *ACS Appl. Mater. Interfaces* **2017**, *9*, 42935−42942.
(87) Brites, C. D. S.; Balabhadra, S.; Carlos, L. D. Lanthanide-Based Thermometers: At the Cutting-Edge of Luminescence Thermometry. *Adv. Opt. Mater.* **2019**, *7*, 1801239.
(88) Akselrod, G. M.; Argyropoulos, C.; Hoang, T. B.; Ciracì, C.; Fang, C.; Huang, J.; Smith, D. R.; Mikkelsen, M. H. Probing the Mechanisms of Large Purcell Enhancement in Plasmonic Nanoantennas. *Nat. Photonics* **2014**, *8*, 835−840.
(89) Schietinger, S.; Aichele, T.; Wang, H. Q.; Nann, T.; Benson, O. Plasmon-Enhanced Upconversion in Single $NaYF_4$:Yb^{3+}/Er^{3+} Codoped Nanocrystals. *Nano Lett.* **2010**, *10*, 134−138.
(90) Saboktakin, M.; Ye, X.; Oh, S. J.; Hong, S. H.; Fafarman, A. T.; Chettiar, U. K.; Engheta, N.; Murray, C. B.; Kagan, C. R. Metal-

https://dx.doi.org/10.1021/acs.jpclett.0c03613
J. Phys. Chem. Lett. 2021, 12, 1520−1541

Enhanced Upconversion Luminescence Tunable through Metal Nanoparticle-Nanophosphor Separation. *ACS Nano* **2012**, *6*, 8758−8766.
(91) Alizadehkhaledi, A.; Frencken, A. L.; van Veggel, F. C. J. M.; Gordon, R. Isolating Nanocrystals with an Individual Erbium Emitter: A Route to a Stable Single-Photon Source at 1550 nm Wavelength. *Nano Lett.* **2020**, *20*, 1018−1022 Correction: **2020** *20* 6222.
(92) Wagenknecht, C.; Li, C. M.; Reingruber, A.; Bao, X. H.; Goebel, A.; Chen, Y. A.; Zhang, Q.; Chen, K.; Pan, J. W. Experimental Demonstration of a Heralded Entanglement Source. *Nat. Photonics* **2010**, *4*, 549−552.
(93) Kolesov, R.; Xia, K.; Reuter, R.; Stöhr, R.; Zappe, A.; Meijer, J.; Hemmer, P. R.; Wrachtrup, J. Optical Detection of a Single Rare-Earth Ion in a Crystal. *Nat. Commun.* **2012**, *3*, 1029.
(94) Shi, S.; Sun, L. D.; Xue, Y. X.; Dong, H.; Wu, K.; Guo, S. C.; Wu, B. T.; Yan, C. H. Scalable Direct Writing of Lanthanide-Doped KMnF 3 Perovskite Nanowires into Aligned Arrays with Polarized Up-Conversion Emission. *Nano Lett.* **2018**, *18*, 2964−2969.
(95) Chen, P.; Song, M.; Wu, E.; Wu, B.; Zhou, J.; Zeng, H.; Liu, X.; Qiu, J. Polarization Modulated Upconversion Luminescence: Single Particle vs. Few-Particle Aggregates. *Nanoscale* **2015**, *7*, 6462−6466.
(96) Rodríguez-Sevilla, P.; Labrador-Páez, L.; Wawrzyńczyk, D.; Nyk, M.; Samoć, M.; Kar, A. K.; Mackenzie, M. D.; Paterson, L.; Jaque, D.; Haro-González, P. Determining the 3D Orientation of Optically Trapped Upconverting Nanorods by in Situ Single-Particle Polarized Spectroscopy. *Nanoscale* **2016**, *8*, 300−308.
(97) Taminiau, T. H.; Stefani, F. D.; Segerink, F. B.; Van Hulst, N. F. Optical Antennas Direct Single-Molecule Emission. *Nat. Photonics* **2008**, *2*, 234−237.
(98) Li, L.; Green, K.; Hallen, H.; Lim, S. F. Enhancement of Single Particle Rare Earth Doped $NaYF_4$:Yb,Er Emission with a Gold Shell. *Nanotechnology* **2015**, *26*, 025101.
(99) Green, K. K.; Wirth, J.; Lim, S. F. Nanoplasmonic Upconverting Nanoparticles as Orientation Sensors for Single Particle Microscopy. *Sci. Rep.* **2017**, *7*, 762.
(100) Xue, Y.; Ding, C.; Rong, Y.; Ma, Q.; Pan, C.; Wu, E.; Wu, B.; Zeng, H. Tuning Plasmonic Enhancement of Single Nanocrystal Upconversion Luminescence by Varying Gold Nanorod Diameter. *Small* **2017**, *13*, 1701155.
(101) He, J.; Zheng, W.; Ligmajer, F.; Chan, C. F.; Bao, Z.; Wong, K. L.; Chen, X.; Hao, J.; Dai, J.; Yu, S. F.; et al. Plasmonic Enhancement and Polarization Dependence of Nonlinear Upconversion Emissions from Single Gold Nanorod@SiO_2@CaF_2:Yb^{3+},Er^{3+} Hybrid Core-Shell-Satellite Nanostructures. *Light: Sci. Appl.* **2017**, *6*, No. e16217.
(102) Chen, L.; Rong, Y.; Ren, M.; Wu, W.; Qin, M.; Pan, C.; Ma, Q.; Liu, S.; Wu, B.; Wu, E.; et al. Selective Polarization Modification of Upconversion Luminescence of $NaYF_4$:Yb^{3+},Er^{3+} Nanoparticles by Plasmonic Nanoantenna Arrays. *J. Phys. Chem. C* **2018**, *122*, 15666−15672.
(103) Ming, T.; Zhao, L.; Chen, H.; Woo, K. C.; Wang, J.; Lin, H. Q. Experimental Evidence of Plasmophores: Plasmon-Directed Polarized Emission from Gold Nanorod - Fluorophore Hybrid Nanostructures. *Nano Lett.* **2011**, *11*, 2296−2303.
(104) Jin, X.; Sang, Y.; Shi, Y.; Li, Y.; Zhu, X.; Duan, P.; Liu, M. Optically Active Upconverting Nanoparticles with Induced Circularly Polarized Luminescence and Enantioselectively Triggered Photopolymerization. *ACS Nano* **2019**, *13*, 2804−2811.
(105) Xiao, W.; Chen, Y.; Han, K.; Shen, X.; Wang, W. Tailoring Spin Angular Momentum of Light: Design Principles for Plasmonic Nanostructures. *Phys. Rev. Appl.* **2020**, *13*, 14029.
(106) Das, A.; Mao, C.; Cho, S.; Kim, K.; Park, W. Over 1000-Fold Enhancement of Upconversion Luminescence Using Water-Dispersible Metal-Insulator-Metal Nanostructures. *Nat. Commun.* **2018**, *9*, 4828.
(107) Liu, J.; Yang, F.; Feng, M.; Wang, Y.; Peng, X.; Lv, R. Surface Plasmonic Enhanced Imaging-Guided Photothermal/Photodynamic Therapy Based on Lanthanide-Metal Nanocomposites under Single 808 nm Laser. *ACS Biomater. Sci. Eng.* **2019**, *5*, 5051−5059.
(108) Syamchand, S. S.; Aparna, R. S.; Sony, G. Plasmonic Enhancement of the Upconversion Luminescence in a Yb^{3+} and Ho^{3+} Co-Doped Gold-ZnO Nanocomposite for Use in Multimodal Imaging. *Microchim. Acta* **2017**, *184*, 2255−2264.
(109) Chen, C. W.; Chan, Y. C.; Hsiao, M.; Liu, R. S. Plasmon-Enhanced Photodynamic Cancer Therapy by Upconversion Nanoparticles Conjugated with Au Nanorods. *ACS Appl. Mater. Interfaces* **2016**, *8*, 32108−32119.
(110) Song, Y.; Liu, G.; Dong, X.; Wang, J.; Yu, W.; Li, J. Au Nanorods@$NaGdF_4$/Yb^{3+},Er^{3+} Multifunctional Hybrid Nanocomposites with Upconversion Luminescence, Magnetism, and Photothermal Property. *J. Phys. Chem. C* **2015**, *119*, 18527−18536.
(111) Wang, C.; Xu, C.; Xu, L.; Sun, C.; Yang, D.; Xu, J.; He, F.; Gai, S.; Yang, P. A Novel Core-Shell Structured Upconversion Nanorod as a Multimodal Bioimaging and Photothermal Ablation Agent for Cancer Theranostics. *J. Mater. Chem. B* **2018**, *6*, 2597−2607.
(112) Soni, A. K.; Joshi, R.; Singh, B. P.; Kumar, N. N.; Ningthoujam, R. S. Near-Infrared- and Magnetic-Field-Responsive $NaYF_4$:Er^{3+}/Yb^{3+}@SiO_2@AuNP@Fe_3O_4 Nanocomposites for Hyperthermia Applications Induced by Fluorescence Resonance Energy Transfer and Surface Plasmon Absorption. *ACS Appl. Nano Mater.* **2019**, *2*, 7350−7361.
(113) Han, S.; Samanta, A.; Xie, X.; Huang, L.; Peng, J.; Park, S. J.; Teh, D. B. L.; Choi, Y.; Chang, Y. T.; All, A. H.; et al. Gold and Hairpin DNA Functionalization of Upconversion Nanocrystals for Imaging and In Vivo Drug Delivery. *Adv. Mater.* **2017**, *29*, 1700244.
(114) Chan, M. H.; Chen, S. P.; Chen, C. W.; Chan, Y. C.; Lin, R. J.; Tsai, D. P.; Hsiao, M.; Chung, R. J.; Chen, X.; Liu, R. S. Single 808 nm Laser Treatment Comprising Photothermal and Photodynamic Therapies by Using Gold Nanorods Hybrid Upconversion Particles. *J. Phys. Chem. C* **2018**, *122*, 2402−2412.
(115) Huang, W. T.; Chan, M. H.; Chen, X.; Hsiao, M.; Liu, R. S. Theranostic Nanobubble Encapsulating a Plasmon-Enhanced Upconversion Hybrid Nanosystem for Cancer Therapy. *Theranostics* **2020**, *10*, 782−796.
(116) Dulkeith, E.; Morteani, A. C.; Niedereichholz, T.; Klar, T. A.; Feldmann, J.; Levi, S. A.; van Veggel, F. C. J. M.; Reinhoudt, D. N.; Möller, M.; Gittins, D. I. Fluorescence Quenching of Dye Molecules near Gold Nanoparticles: Radiative and Nonradiative Effects. *Phys. Rev. Lett.* **2002**, *89*, 203002.
(117) He, E.; Yu, J.; Wang, C.; Jiang, Y.; Zuo, X.; Xu, B.; Wen, J.; Qin, Y.; Wang, Z. Upconversion Luminescence Quenching Mechanism of Single Au Nanoparticles Decorated $NaYF_4$: Yb^{3+}, Er^{3+} Hexagonal Disk. *Mater. Res. Bull.* **2020**, *121*, 110613.
(118) Mendez-Gonzalez, D.; Melle, S.; Calderón, O. G.; Laurenti, M.; Cabrera-Granado, E.; Egatz-Gómez, A.; López-Cabarcos, E.; Rubio-Retama, J.; Díaz, E. Control of Upconversion Luminescence by Gold Nanoparticle Size: From Quenching to Enhancement. *Nanoscale* **2019**, *11*, 13832−13844.
(119) Wu, Y.; Ang, M. J. Y.; Sun, M.; Huang, B.; Liu, X. Expanding the Toolbox for Lanthanide-Doped Upconversion Nanocrystals. *J. Phys. D: Appl. Phys.* **2019**, *52*, 383002.
(120) Ren, W.; Lin, G.; Clarke, C.; Zhou, J.; Jin, D. Optical Nanomaterials and Enabling Technologies for High-Security-Level Anticounterfeiting. *Adv. Mater.* **2020**, *32*, 1901430.
(121) Park, K.; Jung, K.; Kwon, S. J.; Jang, H. S.; Byun, D.; Han, I. K.; Ko, H. Plasmonic Nanowire-Enhanced Upconversion Luminescence for Anticounterfeit Devices. *Adv. Funct. Mater.* **2016**, *26*, 7836−7846.
(122) Park, K.; Park, M.; Jang, H. S.; Park, J. H.; Kim, J.; Cho, Y.; Han, I. K.; Byun, D.; Ko, H. Highly Secure Plasmonic Encryption Keys Combined with Upconversion Luminescence Nanocrystals. *Adv. Funct. Mater.* **2018**, *28*, 1800369.
(123) Liu, H.; Xu, J.; Wang, H.; Liu, Y.; Ruan, Q.; Wu, Y.; Liu, X.; Yang, J. K. W. Tunable Resonator-Upconverted Emission (TRUE)

https://dx.doi.org/10.1021/acs.jpclett.0c03613
J. Phys. Chem. Lett. 2021, 12, 1520−1541

Color Printing and Applications in Optical Security. *Adv. Mater.* **2019**, *31*, 1807900.
(124) Ji, Y.; Xu, W.; Li, D.; Zhou, D.; Chen, X.; Ding, N.; Li, J.; Wang, N.; Bai, X.; Song, H. Semiconductor Plasmon Enhanced Monolayer Upconversion Nanoparticles for High Performance Narrowband Near-Infrared Photodetection. *Nano Energy* **2019**, *61*, 211−220.
(125) Liang, L.; Teh, D. B. L.; Dinh, N. D.; Chen, W.; Chen, Q.; Wu, Y.; Chowdhury, S.; Yamanaka, A.; Sum, T. C.; Chen, C. H.; et al. Upconversion Amplification through Dielectric Superlensing Modulation. *Nat. Commun.* **2019**, *10*, 1391.
(126) Wang, T.; Siu, C. K.; Yu, H.; Wang, Y.; Li, S.; Lu, W.; Hao, J.; Liu, H.; Teng, J. H.; Lei, D. Y.; et al. Influence of Plasmonic Effect on the Upconversion Emission Characteristics of $NaYF_4$ Hexagonal Microrods. *Inorg. Chem.* **2018**, *57*, 8200−8204.
(127) Lee, S. M.; Li, W.; Dhar, P.; Malyk, S.; Wang, Y.; Lee, W.; Benderskii, A.; Yoon, J. High-Performance Flexible Nanostructured Silicon Solar Modules with Plasmonically Engineered Upconversion Medium. *Adv. Energy Mater.* **2015**, *5*, 1500761.
(128) Park, J.; Kim, K.; Jo, E.-J.; Kim, W.; Kim, H.; Lee, R.; Lee, J. Y.; Jo, J. Y.; Kim, M.-G.; Jung, G. Y. Plasmon Enhanced Up-Conversion Nanoparticles in Perovskite Solar Cells for Effective Utilization of near Infrared Light. *Nanoscale* **2019**, *11*, 22813−22819.
(129) Serpone, N.; Emeline, A. V. Semiconductor Photocatalysis - Past, Present, and Future Outlook. *J. Phys. Chem. Lett.* **2012**, *3*, 673−677.
(130) Zhang, Q.; Yang, F.; Xu, Z.; Chaker, M.; Ma, D. Are Lanthanide-Doped Upconversion Materials Good Candidates for Photocatalysis? *Nanoscale Horiz.* **2019**, *4*, 579−591.
(131) Atabaev, T. S.; Molkenova, A. Upconversion Optical Nanomaterials Applied for Photocatalysis and Photovoltaics: Recent Advances and Perspectives. *Front. Mater. Sci.* **2019**, *13*, 335−341.
(132) Li, D.; Yu, S. H.; Jiang, H. L. From UV to Near-Infrared Light-Responsive Metal-Organic Framework Composites: Plasmon and Upconversion Enhanced Photocatalysis. *Adv. Mater.* **2018**, *30*, 1707377.
(133) Kumar, A.; Reddy, K. L.; Kumar, S.; Kumar, A.; Sharma, V.; Krishnan, V. Rational Design and Development of Lanthanide-Doped $NaYF_4$@CdS-Au-RGO as Quaternary Plasmonic Photocatalysts for Harnessing Visible-Near-Infrared Broadband Spectrum. *ACS Appl. Mater. Interfaces* **2018**, *10*, 15565−15581.
(134) Boppella, R.; Marques Mota, F.; Lim, J. W.; Kochuveedu, S. T.; Ahn, S.; Lee, J.; Kawaguchi, D.; Tanaka, K.; Kim, D. H. Plasmon and Upconversion Mediated Broadband Spectral Response in TiO_2 Inverse Opal Photocatalysts for Enhanced Photoelectrochemical Water Splitting. *ACS Appl. Energy Mater.* **2019**, *2*, 3780−3790.
(135) Jiang, Q.; Xie, X.; Riley, D. J.; Xie, F. Harvesting the Lost Photon by Plasmonic Enhanced Hematite-Upconversion Nanocomposite for Water Splitting. *J. Chem. Phys.* **2020**, *153*, 011102.
(136) Zhang, Q.; Liu, Y.; Xu, Z.; Zhao, Y.; Chaker, M.; Ma, D. Optimized Design and Mechanistic Understanding of Plasmon and Upconversion Enhanced Broadband Photocatalysts. *Catal. Today* **2020**, *350*, 25−32.
(137) Ma, Y.; Liu, H.; Han, Z.; Yang, L.; Sun, B.; Liu, J. Raman Scattering and Plasmonic Photocatalysis of Single Particles of $NaYF_4$:Yb, Er@Ag under near-Infrared Laser Excitation. *Analyst* **2014**, *139*, 5983−5988.
(138) Zhang, J.; Huang, Y.; Jin, L.; Rosei, F.; Vetrone, F.; Claverie, J. P. Efficient Upconverting Multiferroic Core@Shell Photocatalysts: Visible-to-Near-Infrared Photon Harvesting. *ACS Appl. Mater. Interfaces* **2017**, *9*, 8142−8150.
(139) Maji, S. K.; Kim, D. H. $AgInS_2$-Coated Upconversion Nanoparticle as a Photocatalyst for Near-Infrared Light-Activated Photodynamic Therapy of Cancer Cells. *ACS Appl. Bio Mater.* **2018**, *1*, 1628−1638.
(140) Tian, Q.; Yao, W.; Wu, W.; Jiang, C. NIR Light-Activated Upconversion Semiconductor Photocatalysts. *Nanoscale Horizons* **2019**, *4*, 10−25.
(141) Sahu, S. P.; Cates, S. L.; Kim, H. Il; Kim, J. H.; Cates, E. L. The Myth of Visible Light Photocatalysis Using Lanthanide Upconversion Materials. *Environ. Sci. Technol.* **2018**, *52*, 2973−2980.
(142) Andrew, P.; Barnes, W. L. Forster Energy Transfer in an Optical Microcavity. *Science* **2000**, *290*, 785−788.
(143) Gonzaga-Galeana, J. A.; Zurita-Sánchez, J. R. A Revisitation of the Förster Energy Transfer near a Metallic Spherical Nanoparticle: (1) Efficiency Enhancement or Reduction? (2) The Control of the Förster Radius of the Unbounded Medium. (3) The Impact of the Local Density of States. *J. Chem. Phys.* **2013**, *139*, 244302.
(144) De Dood, M. J. A.; Knoester, J.; Tip, A.; Polman, A. Förster Transfer and the Local Optical Density of States in Erbium-Doped Silica. *Phys. Rev. B: Condens. Matter Mater. Phys.* **2005**, *71*, 115102.
(145) Blum, C.; Zijlstra, N.; Lagendijk, A.; Wubs, M.; Mosk, A. P.; Subramaniam, V.; Vos, W. L. Nanophotonic Control of the Förster Resonance Energy Transfer Efficiency. *Phys. Rev. Lett.* **2012**, *109*, 203601.
(146) Yang, Y.; Liao, J.; Yang, Z.; Lai, S.; Shao, B.; Li, J.; Qiu, J.; Song, Z. Upconversion Emission Enhancement of NaYF4:Yb,Er Nanoparticles by Coupling Silver Nanoparticle Plasmons and Photonic Crystal Effects. *J. Phys. Chem. C* **2014**, *118*, 17992−17999.
(147) Shao, B.; Yang, Z.; Wang, Y.; Li, J.; Yang, J.; Qiu, J.; Song, Z. Coupling of Ag Nanoparticle with Inverse Opal Photonic Crystals as a Novel Strategy for Upconversion Emission Enhancement of $NaYF_4$:Yb^{3+}, Er^{3+} Nanoparticles. *ACS Appl. Mater. Interfaces* **2015**, *7*, 25211−25218.
(148) Yin, Z.; Li, H.; Xu, W.; Cui, S.; Zhou, D.; Chen, X.; Zhu, Y.; Qin, G.; Song, H. Local Field Modulation Induced Three-Order Upconversion Enhancement: Combining Surface Plasmon Effect and Photonic Crystal Effect. *Adv. Mater.* **2016**, *28*, 2518−2525.
(149) Gao, Y.; Murai, S.; Zhang, F.; Tamura, S.; Tomita, K.; Tanaka, K. Enhancing Upconversion Photoluminescence by Plasmonic-Photonic Hybrid Mode. *Opt. Express* **2020**, *28*, 886−897.
(150) Wang, Z.; Christiansen, J.; Wezendonk, D.; Xie, X.; Van Huis, M. A.; Meijerink, A. Thermal Enhancement and Quenching of Upconversion Emission in Nanocrystals. *Nanoscale* **2019**, *11*, 12188−12197.
(151) Zhou, D.; Li, D.; Zhou, X.; Xu, W.; Chen, X.; Liu, D.; Zhu, Y.; Song, H. Semiconductor Plasmon Induced Up-Conversion Enhancement in $mCu_{2-X}S$@SiO_2@Y_2O_3:Yb^{3+}/Er^{3+} Core-Shell Nanocomposites. *ACS Appl. Mater. Interfaces* **2017**, *9*, 35226−35233.
(152) Li, J.; Zhang, W.; Lu, C.; Lou, Z.; Li, B. Nonmetallic Plasmon Induced 500-Fold Enhancement in the Upconversion Emission of the UCNPs/WO_{3-x} Hybrid. *Nanoscale Horiz.* **2019**, *4*, 999−1005.
(153) Zhou, D.; Li, D.; Zhou, X.; Xu, W.; Chen, X.; Liu, D.; Zhu, Y.; Song, H. Semiconductor Plasmon Induced Upconversion Enhancement in $MCu_{2-x}S$@SiO_2@Y_2O_3:Yb^{3+},Er^{3+} Core-Shell Nanocomposites. *ACS Appl. Mater. Interfaces* **2017**, *9*, 35226−35233.
(154) Liu, J.; Zou, Z.; Shi, F.; Song, X.; Zhang, H.; Zhang, H.; Song, X.; Zhao, X.; Wang, Z.; Kang, J. Construction of a Novel Pitaya-like Cs_xWO_3@$NaYF_4$:Yb,Er Particles with Simultaneous Colour Tuning and Upconversion Luminescence Enhancement. *J. Alloys Compd.* **2021**, *854*, 157139.
(155) Zhou, D.; Liu, D.; Xu, W.; Yin, Z.; Chen, X.; Zhou, P.; Cui, S.; Chen, Z.; Song, H. Observation of Considerable Upconversion Enhancement Induced by $Cu_{2-X}S$ Plasmon Nanoparticles. *ACS Nano* **2016**, *10*, 5169−5179.

https://dx.doi.org/10.1021/acs.jpclett.0c03613
J. Phys. Chem. Lett. 2021, 12, 1520−1541